AGU PUBLICATIONS

JGR

Journal of Geophysical Research: Solid Earth

RESEARCH ARTICLE
10.1002/2013JB010686

Key Points:
- High salinity and temperature gradients are present at a Gulf of Mexico vent
- A dynamic model of hydrate formation can explain these observations

Supporting Information:
- Readme
- Movie S1

Correspondence to:
A. J. Smith,
andrew.j.smith.6022@gmail.com

Citation:
Smith, A. J., P. B. Flemings, X. Liu, and K. Darnell (2014), The evolution of methane vents that pierce the hydrate stability zone in the world's oceans, *J. Geophys. Res. Solid Earth*, *119*, 6337–6356, doi:10.1002/2013JB010686.

Received 11 SEP 2013
Accepted 8 JUL 2014
Accepted article online 16 JUL 2014
Published online 4 AUG 2014

The evolution of methane vents that pierce the hydrate stability zone in the world's oceans

Andrew J. Smith[1,2,3,4], Peter B. Flemings[1,2,3], Xiaoli Liu[5], and Kristopher Darnell[1,2,3]

[1]Jackson School of Geosciences, University of Texas at Austin, Austin, Texas, USA, [2]Institute for Geophysics, University of Texas at Austin, Austin, Texas, USA, [3]Bureau of Economic Geology, University of Texas at Austin, Austin, Texas, USA, [4]Centre for Arctic Gas Hydrate, Environment and Climate, University of Tromsø, Tromsø, Norway, [5]Anadarko Petroleum Corporation, Geological Technology, Houston, Texas, USA

Abstract We present a one-dimensional model that couples the thermodynamics of hydrate solidification with multiphase flow to illuminate how gas vents pierce the hydrate stability zone in the world's oceans. During the propagation phase, a free-gas/hydrate reaction front propagates toward the seafloor, elevating salinity and temperature to three-phase (gas, liquid, and hydrate) equilibrium. After the reaction front breaches the seafloor, the temperature gradient in the gas chimney dissipates to background values, and salinity increases to maintain three-phase equilibrium. Ultimately, a steady state is reached in which hydrate formation occurs just below the seabed at a rate necessary to replace salt loss. We show that at the Ursa vent in the Gulf of Mexico, the observed salinity and temperature gradients can be simulated as a steady state system with an upward flow of water equal to 9.5 mm yr^{-1} and a gas flux no less than 1.3 kg m^{-2} yr^{-1}. Many of the world's gas vents may record this steady state behavior, which is characterized by elevated temperatures and high salinities near the seafloor.

1. Introduction

Gas hydrate is an ice-like compound that contains methane and other light hydrocarbon gases in a lattice of water molecules [*Sloan*, 1998]. It is naturally found along continental margins in water depths > ~400 m, where high pressures, low temperatures, and ample supplies of gas are present [*Kvenvolden*, 1993]. Gas hydrates may host economic quantities of natural gas [*Milkov and Sassen*, 2002]. Their dissociation may have contributed to past environmental change [*Dickens*, 2003; *Kennett et al*., 2000] and may be causing ongoing methane release to the ocean and atmosphere in the Arctic [*Berndt et al*., 2014; *Marín-Moreno et al*., 2013; *Westbrook et al*., 2009] and offshore the eastern United States [*Phrampus and Hornbach*, 2012].

Gas vents that pierce the hydrate stability zone (HSZ) are a ubiquitous feature of the world's oceans, and they have received intense focus in the last decade. A negative-polarity seismic reflection is often present at the seafloor of vents [*Evans et al*., 2007; *Kohl and Roberts*, 1994; *Reilly and Flemings*, 2010; *Seldon and Flemings*, 2005]. This negative-polarity event represents a significant decrease in acoustic impedance at the water-seafloor interface and most likely records the presence of free gas at or near the seafloor. High-temperature gradients [*Hornbach et al*., 2005; *Pape et al*., 2011; *Römer et al*., 2012; *Ruppel et al*., 2005b] and elevated salinities [*Liu and Flemings*, 2006; *Milkov et al*., 2004; *Paull et al*., 2005; *Ruppel et al*., 2005b; *Sahling et al*., 2009] are also present just below the seafloor at vents. These vents are provocative because a traditional view of the HSZ has been that methane should not be able to pass through the HSZ because temperature and salinity are assumed too low to allow it.

We use the Ursa vent as a characteristic vent throughout this paper. It lies in ~1070 m water depth at lease blocks MC852/853 in the northern Gulf of Mexico (GoM) (Figure 1a). There is a strong, negative-polarity seismic reflection beneath the vent that we interpret records a negative impedance contrast, marking the boundary between hydrate and water above and gas and water below: it is the bottom-simulating reflector (BSR) (Figure 2) [*Bangs et al*., 1993; *Shipley et al*., 1979]. The BSR rises rapidly at the vent's boundaries and shoals all the way to the seafloor at some locations beneath the vent edifice (Figures 1a and 2). Salinity and temperature gradients on the vent are elevated significantly compared to background values (Figures 1b and 1c), causing the base of the HSZ to be up to 5.7 m below seafloor (mbsf) for pure methane and 28 mbsf for the average gas composition measured at the vent [*Ruppel et al*., 2005b; *Sassen et al*., 2001]. Gas from hydrates

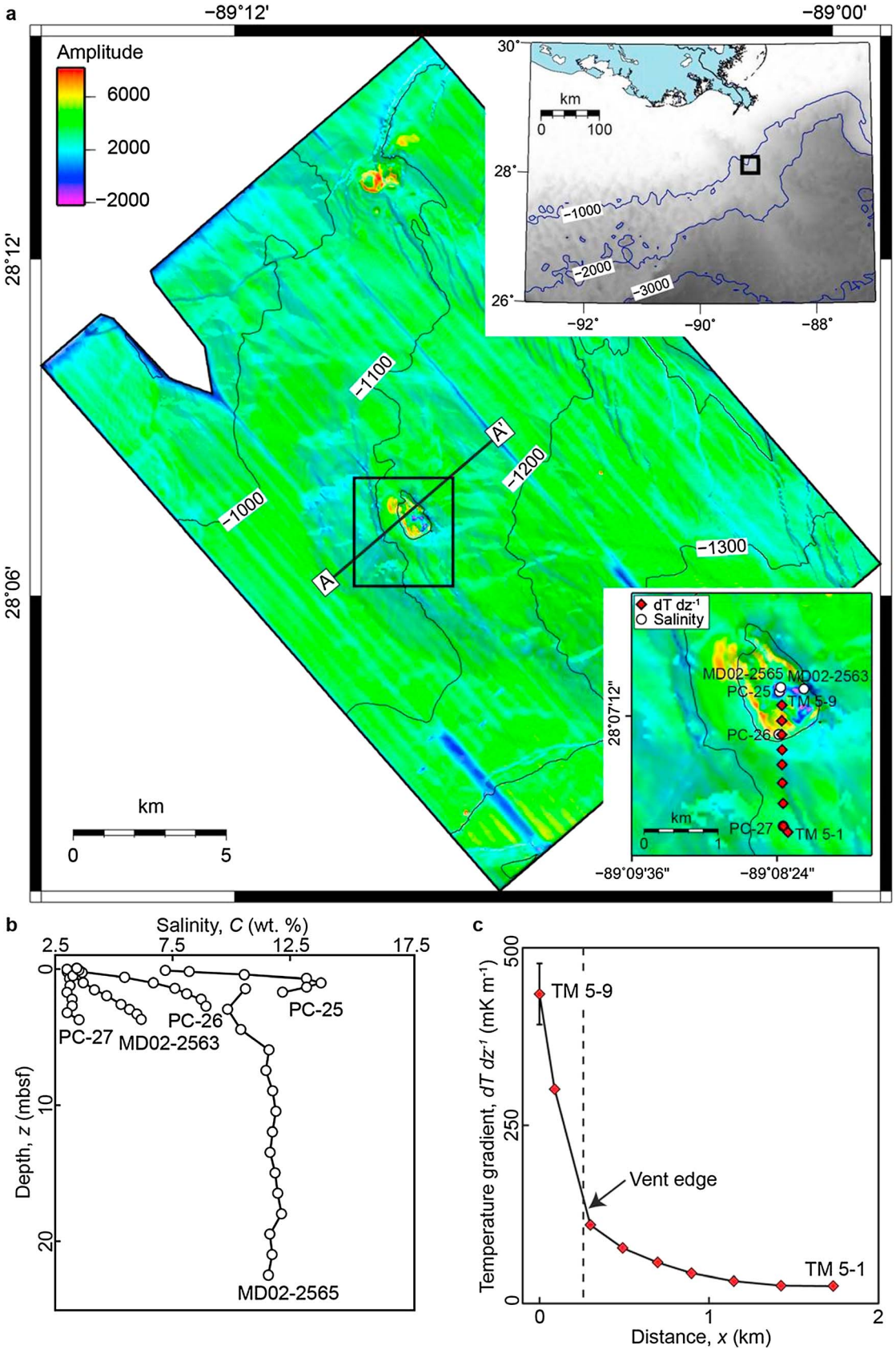

Figure 1

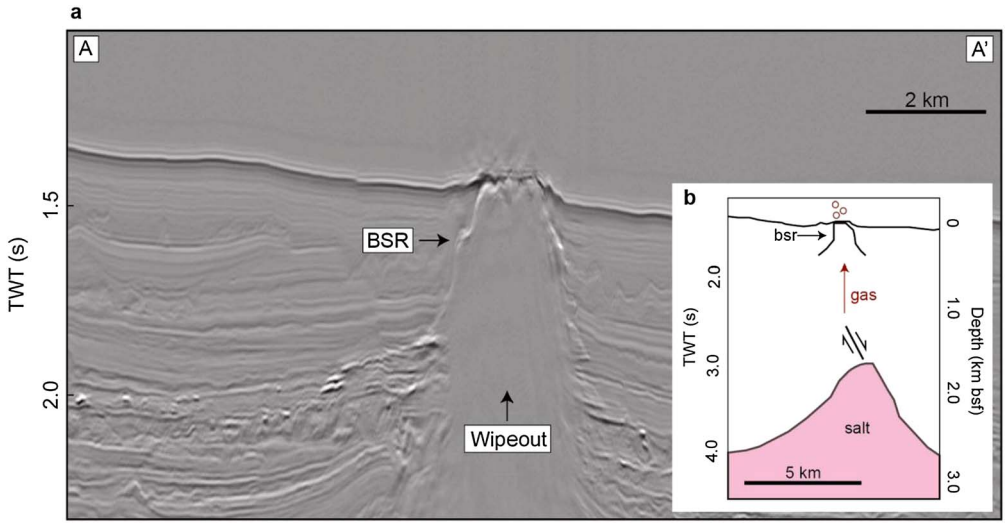

Figure 2. (a) Seismic reflection profile through the MC852/853 vent (A-A′ in Figure 1). A vertical wipeout zone beneath the vent is interpreted to record the presence of gas. The BSR rises rapidly at the vent edges and is horizontal within a few meters of the seafloor beneath the vent edifice. (b) Cartoon of the deep plumbing feeding the vent. Salt/fault geometry and depth are constrained from deeper seismic reflection profiles presented in another publication [*Smith et al.*, 2014]. A normal fault is clearly imaged just above the salt body but cannot be followed to the seafloor through the gas wipeout zone. A stratigraphic summary of the Mars-Ursa minibasin can be found in *Sawyer et al.* [2007].

recovered at the vent is on average 75.1% C_1, 7.5% C_2, 11.2% C_3, 5.5% i-C_4, and 0.5% nC_4 [*Ruppel et al.*, 2005b; *Sassen et al.*, 2001; *Winters et al.*, 2007]. Gas bubbles are released upon slight physical disturbance of the mound, and fluid flow from the vent sustains a chemosynthetic biological community [*MacDonald et al.*, 2003].

Although the coexistence of gas hydrates, free-gas expulsion, an uplifted BSR, and high salinities and temperatures has been well documented at Ursa and other vents, conclusive evidence of the origin of these phenomena has remained elusive. Until now, it has generally been assumed that high salinities and temperatures near the seafloor are generated via the upward flow of warm, salty fluids from depth [e.g., *Hanor and Mercer*, 2010; *Ruppel et al.*, 2005b; *Wood et al.*, 2002]. In these studies, the vertical expulsion of hot, salty fluids results in the shifting of the base of the HSZ to the seafloor. This approach is supported by seismic data which show that vents are fed by reservoirs that flank salt diapirs [*Reilly and Flemings*, 2010; *Seldon and Flemings*, 2005], implying that salty fluids may possibly be produced via dissolution of salt bodies at depth. Furthermore, concave-down geochemical profiles provide evidence for upward advective flow [*Paull et al.*, 2005; *Reitz et al.*, 2007; *Ruppel et al.*, 2005b].

Models of advective aqueous flux, however, cannot fully explain both the high-temperature gradients and relatively high salinities observed at vents [*Hornbach et al.*, 2005; *Smith et al.*, 2014]. The typical approach used to estimate aqueous flux at vents is based on the salinity gradient, which predicts water flow of the order of 1–100 mm yr^{-1} [*Egeberg*, 2000; *Reitz et al.*, 2007; *Schmidt et al.*, 2005; *Smith et al.*, 2014]. These fluxes are not sufficient to explain the high-temperature gradients recorded [*Hornbach et al.*, 2005; *Smith et al.*, 2014], and only with an interpretation of an extraordinarily large hydrocarbon flux (41–190 kg m^{-2} yr^{-1}) can the observed temperatures be reconciled [*Smith et al.*, 2014].

An alternative mechanism for elevating salinity and temperature is hydrate solidification. When hydrate crystallizes, salinity is generated via the exclusion of salt [*Liu and Flemings*, 2007], and temperature is elevated

Figure 1. (a) Seafloor seismic amplitudes with shaded structural relief of the Ursa Basin. Contours are in mbsl (converted from two-way traveltime assuming an acoustic velocity of 1.5 km s^{-1}). The Ursa vent at lease blocks MC852/853 (black box) is located in ~1070 m water depth and is ~220 km South Southeast (SSE) of New Orleans. High seafloor amplitudes (red/yellow) likely record the presence of gas hydrate or carbonate. Negative amplitudes (purple/blue) indicate areas where the bottom-simulating reflector (BSR) rises all the way to the seafloor (Figure 2). Lower inset map shows the locations of temperature-gradient, piston-core, and box-core measurements on the vent [*Paull et al.*, 2005; *Ruppel et al.*, 2005b]. (b) Observed subseabed salinities at Ursa [*Paull et al.*, 2005; *Ruppel et al.*, 2005b]. Chloride profiles MD02-2563 and MD02-2565 are converted to salinity by assuming a Cl^- (mM) to salinity (wt %) ratio of ~19, which is the average ratio observed by *Ruppel et al.* [2005a] at the MC852/853 vent. (c) Temperature gradients measured in the first ~3 mbsf [*Ruppel et al.*, 2005b]. TM 5–9 and TM 5–8 are the only two measurements taken on the vent edifice, and they record high-temperature gradients of 435 mK m^{-1} and 301 mK m^{-1}, respectively.

from the release of latent heat [*Cathles and Chen*, 2004; *Liu and Flemings*, 2009]. When transported in the gaseous phase, methane and other light natural gasses will have hydrate-formation rates that are high enough to rapidly elevate salinity and form three-phase (gas, liquid, and hydrate) chimneys within the regional hydrate stability zone (RHSZ) [*Liu and Flemings*, 2006, 2007]. Numerical simulations of this process produce salinity profiles that increase from the base of the RHSZ to the seafloor [*Liu and Flemings*, 2006, 2007], and geochemical profiles measured at Ursa and other vents exhibit such increases in salinity with decreasing depth [*Paull et al*., 2005; *Ruppel et al*., 2005b] (Figure 1b).

Here we present a model to describe hydrate formation at the Ursa vent in the GoM. We extend the work of *Liu and Flemings* [2006, 2007] by accounting for the latent heat released during hydrate formation. First, we present a simple equilibrium model of hydrate formation to describe how high salinities and temperatures can extend the three-phase zone from the base of the RHSZ to the seafloor. We then use a similar dynamic multiphase-flow model of hydrate formation as *Liu and Flemings* [2007] to simulate temperature, salinity, gas saturation, hydrate saturation, and pressure during the upward migration of gas through the RHSZ. We explore how different gas and water fluxes affect the result.

Our results suggest that gas vents evolve through three distinct phases. First, hydrate solidification from the upward flow of gas will elevate salinity and temperature to three-phase equilibrium within the RHSZ. With time, a propagating free-gas/hydrate reaction front breaches the seafloor, a gas chimney forms, and gas fluxes from the base of the RHSZ into the ocean. After breaching, the temperature gradient in the gas chimney dissipates, and salinity increases to maintain three-phase equilibrium. When there is no water flow, the system eventually reaches a steady state in which hydrate formation occurs just below the seafloor at a rate necessary to replace diffuse salt loss. When there is water flow, during the steady state phase, hydrate continually forms due to constant upward flow of water. Many vents around the world may be exhibiting this final phase which is characterized by high salinities and elevated temperature gradients just below the seafloor.

2. Simplified Approach to Predict Salinity and Temperature During Hydrate Formation

We model pressure and temperature conditions characteristic of the Ursa vent. The vent is 1070 m below sea level (mbsl). The seafloor temperature is ~5°C, and the background geothermal gradient is initially ~25 mK m^{-1} [*Paull et al*., 2005; *Ruppel et al*., 2005b]. We assume that the sediment column is hydrostatically pressured, that methane is the only natural gas present, and that pore water initially has seawater salinity (weight 3.5%). Under these conditions, the base of the RHSZ is ~435 mbsf. In reality, elevated pore pressures likely exist just below the seafloor of the vent [*Flemings et al*., 2008]. These overpressures, however, will not significantly affect the depth of the RHSZ.

We initially develop an equilibrium model for hydrate formation, which ignores volume expansion, chemical diffusion, thermal conduction, and transport of the liquid phase. In this model, the hydrate reservoir is a closed system for salt, water, and energy, but not gas. This approximation of hydrate formation describes how hydrate saturation, salinity, and temperature evolve in the sediment column when free gas is supplied from below. The salinity and temperature necessary to shift the region of three-phase hydrate stability upward from the base of the RHSZ are calculated using the liquid-hydrate ($l+h$) and liquid-gas ($l+g$) methane solubility curves [*Duan et al*., 1992; *Henry et al*., 1999].

If latent heat of hydrate crystallization is ignored, the hydrate saturation (S_h) at a given depth below seafloor (z) necessary to elevate salinity to three-phase equilibrium (C_{eq}) can be expressed as (Figure 3)

$$S_h(z) = 1 - \frac{C_i}{C_{eq}(z)}, \tag{1}$$

where C_i is seawater salinity (3.5 wt %) [*Liu and Flemings*, 2006] (Table 1). In order to generate three-phase equilibrium through the RHSZ, salinity increases linearly from seawater salinity at the base of the RHSZ to 15 wt % at the seafloor (Figure 3b). To elevate these salinities, hydrate saturations increase upward from the base of the RHSZ to 0.77 at the seafloor (Figure 3a). Since latent heat is ignored, the temperature gradient follows the background geothermal gradient (Figure 3c).

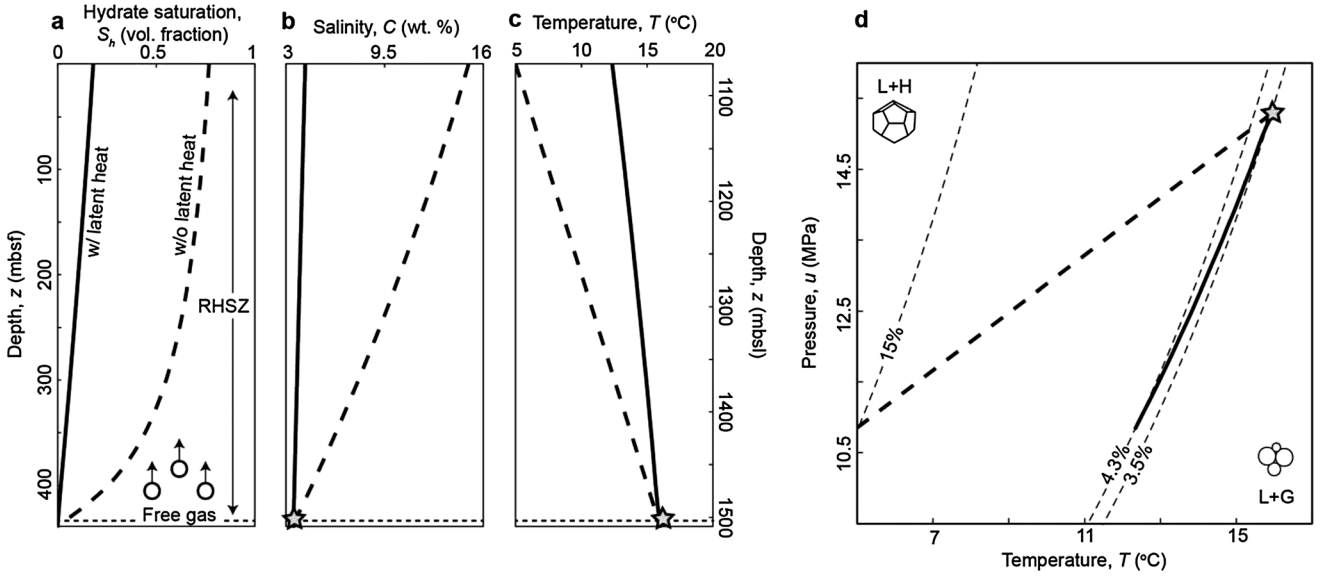

Figure 3. Simplified equilibrium model that simulates hydrate formation in a closed system. Two cases are considered: one in which latent heat is ignored (dashed line) [*Liu and Flemings*, 2006] and one in which latent heat is accounted for (solid line). (a) Hydrate saturations in the sediment column. (b) Salinity is elevated via the exclusion of salt during hydrate formation. (c) Heat is also released due to the latent heat of hydrate crystallization. This causes modeled temperatures to be higher than the background geothermal gradient. If latent heat is ignored, simulated temperatures follow the geothermal gradient. (d) Hydrate stability pressure-temperature phase diagram for waters of 3.5 wt %, 4.3 wt %, and 15 wt % salinity. If latent heat is ignored, salinity needs to be elevated to 15 wt % in order to displace the three-phase ($l+g+h$) boundary to the seafloor (~10.8 MPa). If latent heat is considered, salinity needs to be elevated to only 4.3 wt % to generate three-phase equilibrium to the seafloor.

The temperature change (ΔT) resulting from release of latent heat associated with a change in hydrate saturation (ΔS_h) can be expressed as

$$\Delta T = \frac{L\phi_o\rho_h\Delta S_h}{\rho_b c_b}, \tag{2}$$

where L is the latent heat of hydrate crystallization (421 kJ kg^{-1}) [*Cathles and Chen*, 2004], ϕ_o is the porosity in the absence of hydrate (0.5) [*Flemings et al.*, 2006], and ρ_h is the hydrate density (912 kg m^{-3}). Bulk density (ρ_b) and heat capacity (c_b) are expressed as follows:

$$\rho_b = (1-\phi_o)\rho_s + \phi_o\rho_h S_h + \phi_o\rho_w(1-S_h), \tag{3}$$

$$c_b = (1-\phi_o)c_s + \phi_o c_h S_h + \phi_o c_w(1-S_h), \tag{4}$$

where ρ_s and ρ_w are densities of sediment (2650 kg m^{-3}) and seawater (1035 kg m^{-3}) and c_h, c_s, and c_w are heat capacities of hydrate (2100 J K^{-1} kg^{-1}), sediment (1381 J K^{-1} kg^{-1}), and seawater (4200 J K^{-1} kg^{-1}). Substituting equations (3) and (4) into equation (2) and assuming temperature initially increases linearly from seafloor temperature (T_o) with depth (z) according to the geothermal gradient (dT dz^{-1}), the hydrate saturation (S_h) at a given depth (z) necessary to elevate temperature to three-phase equilibrium (T_{eq}) can be expressed as

$$S_h(z) = \left(T_{eq}(z) - T_o - z\frac{dT}{dz}\right)\frac{((1-\phi_o)\rho_s + (\phi_o S_h\rho_h) + (\phi_o\rho_w)(1-S_h))((1-\phi_o)c_s + (\phi_o S_h c_h) + (\phi_o c_w)(1-S_h))}{L\phi_o\rho_h}. \tag{5}$$

Equations (1) and (5) are used together to calculate the hydrate saturation at a given depth necessary to elevate both salinity and temperature to three-phase equilibrium (Figure 3). In this closed system, hydrate saturations increase linearly from the base of the HSZ to 0.18 at the seafloor (Figure 3a). Salinity also increases linearly upward through the RHSZ to 4.3 wt % at the seafloor (Figure 3b). Temperature decreases with shallower depths, but at a smaller gradient than the background geothermal gradient (Figure 3c). This simple equilibrium model is an end-member model of perfect insulation.

For a given change in hydrate saturation, the effect of temperature on hydrate stability is much more substantial than that of salinity. For example, a change in hydrate saturation of 0.1 elevates salinity to ~3.9 wt % and

Table 1. Nomenclature

Symbol	Name	Dimension[a]
a	Salinity gradient	L^{-1}
b	Background water salinity	dimensionless
C	Salinity	dimensionless
C_{eq}	Equilibrium salinity at depth z	dimensionless
$c_{h,s,w,b}$	Heat capacity (hydrate, sediment, water, and bulk)	$L^2 t^{-2} T^{-1}$
C_i	Initial (seawater) salinity	dimensionless
C_{LN}	Composition (salt) in liquid	dimensionless
$\overline{C}_N$	Average composition of salt	dimensionless
c_β	Heat capacity of phase β	$L^2 t^{-2} T^{-1}$
$D_{l0}{}^K$	Molecular diffusion coefficient of component K in free water	$L^2 t^{-1}$
$dT\ dz^{-1}$	Thermal gradient	$T L^{-1}$
e	Energy component	na
$F_b{}^m$	Basal mass flux of methane	$M L^{-2} t^{-1}$
g	Acceleration due to gravity	$L t^{-2}$
h	Hydrate phase	na
h_β	Specific enthalpy of phase β	$L^2 t^{-2}$
k	Permeability	L^2
K	Component K (methane (m), salt (s), and water (w))	na
$k_{r\beta}$	Relative permeability of phase β	Dimensionless
l	Liquid phase	na
$l+h$	Liquid hydrate	na
$l+g$	Liquid-gas	na
L	Latent heat of hydrate crystallization	$L^2 t^{-2}$
m	Methane component	na
q^e	Generation rate of energy	$M L^2 t^{-3}$
Q_e	Background heat flow	$M t^{-3}$
q_g	Gas flux	$M L^{-2} t^{-1}$
q^K	Source term of component K	$M L^{-3} t^{-1}$
q_w	Water flux	$M L^{-2} t^{-1}$
q_w	Darcy water flux	$L^{-1} t^{-1}$
s	Salt component	na
S_v	Lithostatic stress	$M t^{-2} L^{-1}$
S_β	Saturation of phase β	dimensionless
T	Temperature	T
t	Time	t
T_b	Basal temperature	T
T_{eq}	Equilibrium temperature at depth z	T
T_o	Initial (seafloor) temperature	T
u	Pressure	$M t^{-2} L^{-1}$
u_h	Hydrostatic pressure	$M t^{-2} L^{-1}$
u_β	Pressure of phase β	$M t^{-2} L^{-1}$
v	Vapor phase	na
V_o	Liquid velocity	$L t^{-1}$
w	Water component	na
x	Horizontal distance	L
$X_h{}_K$	Mass of hydrate	M
$X_\beta{}^K$	Mass fraction of component K in phase β	dimensionless
z	Depth	L
Z_{HSZ}	Thickness of the HSZ	L
Δz	Grid spacing	L
β	Phase (liquid, vapor, and hydrate)	na
ϕ	Porosity (dependent on hydrate saturation)	dimensionless
ϕ_o	Porosity in the absence of hydrate	dimensionless
λ	Bulk thermal conductivity	$M L t^{-3} T^{-1}$
λ_s	Thermal conductivity of grain	$M L t^{-3} T^{-1}$
λ_β	Thermal conductivity of phase β	$M L t^{-3} T^{-1}$
μ_β	Viscosity of phase β	$M L^{-1} t^{-1}$

increases temperature by ~4°C. By itself, this salinity change shifts the base of the HSZ from 435 mbsf to 420 mbsf. Conversely, a temperature change of 4°C, without any change in salinity, shifts the base of the HSZ from 435 mbsf to 215 mbsf. The heat added by hydrate formation is therefore a significant fraction of normal heat flow and may cause significant deviation from the linear thermal gradient in a marine gas-hydrate system.

3. Dynamic Model of Hydrate Formation

3.1. Model Description

We now use a one-dimensional, multicomponent, multiphase, fluid- and heat-flow model developed by *Liu and Flemings* [2007] to address this problem. We simulate temperature, salinity, hydrate saturation, gas saturation, methane concentration, and pressure during hydrate formation and free-gas migration for a hydrate system fed from below by gas. At Ursa, thermogenic gas is sourced from below via secondary hydrocarbon migration along faults above a salt body (Figure 2b) [*Smith et al.*, 2014]. Although we use Ursa as a specific example, this model can be applied to any hydrate system where gas and water are transported to the HSZ from below.

3.1.1. Assumptions

We make the same assumptions as *Liu and Flemings* [2007]: (1) The foremost assumption is that there is local thermodynamic equilibrium; in marine sediments, this is justified because hydrate forms rapidly (hours to days) as shown by experiments [*Linga et al.*, 2012; *Zatsepina and Buffett*, 2003] and field studies [*Rehder et al.*, 2002]. (2) Darcy's law describes multiphase fluid flow in a uniform porous medium. (3) There is no sedimentation or erosion. (4) Gas and water are supplied from beneath the RHSZ. (5) Methane is the only hydrate-forming gas. (6) Diffusion is only considered in the liquid phase, because diffusion of CH_4 within hydrate and free gas is negligible

Table 1. (continued)

Symbol	Name	Dimension[a]
θ	Tortuosity	dimensionless
$\rho_{h,s,w,b}$	Density (hydrate, sediment, water, and bulk)	ML^{-3}
ρ_β	Density of phase β	ML^{-3}
$\bar{\rho}$	Average density of pore volume	ML^{-3}

[a]T = temperature; M = mass; t = time; L = length; na = not applicable.

[*Liu and Flemings*, 2007]. (7) Methane is assumed to be the only component in the vapor phase, because the amount of water in the vapor phase is small [*Duan et al*., 1992]. (8) Salt is confined to the liquid phase. (9) Hydrate is a solid phase and only two-phase (gas + water) capillary pressure is considered.

3.1.2. Governing Equations and Numerical Solution

We treat the hydrate reservoir as a continuum of sediment grains, fluids, and solid hydrate [*Liu and Flemings*, 2007]. We conserve mass for water, methane, and salt, and we conserve energy [*Liu and Flemings*, 2007]. The mass balance of methane (superscript *m*) is described as

$$\phi\frac{\partial\left(\sum_{\beta=l,v,h}\rho_\beta S_\beta X_\beta^m\right)}{\partial t}-\sum_{\beta=l,v}\left\{\mathrm{div}\frac{kk_{r\beta}}{\mu_\beta}\rho_\beta X_\beta^m\left(\nabla u_\beta-\rho_\beta g\right)\right\}-\mathrm{div}\frac{\phi}{\theta^2}D_{l0}^m\rho_l\nabla X_l^m-q^m=0, \quad (6)$$

where ρ_β is the density of phase β (liquid (l), vapor (v), and hydrate (h)), S_β is the saturation of phase β, ${\beta^m}_\beta$ is the mass fraction of methane in phase β, t is time, k is permeability, $k_{r\beta}$is the relative permeability of phase β, u_β is the pressure of phase β, g is the acceleration due to gravity, ϕ is porosity, θ^2 is tortuosity defined as ϕ^{-1} [*Torres et al*., 2004], ${D^m}_{l0}$ is the molecular diffusion coefficient of methane in free water, and q^m is the source term of methane. The mass-balance equation for water (superscript *w*) is

$$\phi\frac{\partial\left(\sum_{\beta=l,h}\rho_\beta S_\beta X_\beta^w\right)}{\partial t}-\sum_{\beta=l,v}\left\{\mathrm{div}\frac{kk_{r\beta}}{\mu_\beta}\rho_\beta X_\beta^w\left(\nabla u_\beta-\rho_\beta g\right)\right\}-\mathrm{div}\frac{\phi}{\theta^2}D_{l0}^w\rho_l\nabla X_l^w-q^w=0. \quad (7)$$

The mass balance for salt (superscript *s*) is

$$\phi\frac{\partial\left(\sum_{\beta=l}\rho_\beta S_\beta X_\beta^s\right)}{\partial t}-\sum_{\beta=l,v}\left\{\mathrm{div}\frac{kk_{r\beta}}{\mu_\beta}\rho_\beta X_\beta^s\left(\nabla u_\beta-\rho_\beta g\right)\right\}-\mathrm{div}\frac{\phi}{\theta^2}D_{l0}^s\rho_l\nabla X_l^s-q^s=0. \quad (8)$$

The energy-balance equation (superscript *e*) is

$$\frac{\partial T}{\partial t}\left((1-\phi)\rho_s c_s+\sum_{\beta=l,v,h}\phi\rho_\beta S_\beta c_\beta\right)-\sum_{\beta=l,v}\rho_\beta c_\beta\frac{kk_{r\beta}}{\mu_\beta}\left(\nabla u_\beta-\rho_\beta g\right)\nabla T-\phi\rho_h L\frac{\partial S_h}{\partial t}-\mathrm{div}\{\lambda\nabla T\}-q^e=0, \quad (9)$$

where λ is bulk thermal conductivity:

$$\lambda=(1-\phi)\lambda_s+\phi(S_h\lambda_h+S_l\lambda_l+S_v\lambda_v). \quad (10)$$

This approach is identical to that described by *Liu and Flemings* [2007], except that we account for the latent heat of hydrate formation/disassociation (L) (third term of equation (9)) as is done in *Liu and Flemings* [2009], and we specifically consider the effect of a water flux from below.

The mass-balance equations are discretized in space and time using the block-centered finite-difference method [*Liu and Flemings*, 2007]. Each parameter is calculated at block centers. Different physical parameters require different interface weighting algorithms. For example, upstream weighting is used to calculate the phase mobility, and harmonic weighting is used to calculate the intrinsic permeability [*Liu and Flemings*, 2007]. The accumulation terms are discretized in time using a first-order finite-difference approximation. We evaluate flux and sink/source terms at each new time level to avoid numerical instability [*Liu and Flemings*, 2007].

3.1.3. Physical Processes

We calculate equilibrium conditions for the hydrate system using the liquid-gas ($l+g$) methane solubility curve [*Duan et al*., 1992] and the liquid-hydrate ($l+h$) methane solubility curve [*Henry et al*., 1999]. We assume hydrate formation is pore filling, which results in more rapid permeability reduction than in a pore-coating

Table 2. Physical Parameters Used for Dynamic Multiphase-Flow Model

Symbol	Parameter	Value (Unit)	Reference
c_g	Heat capacity of methane gas	3500 ($J K^{-1} kg^{-1}$)	*Liu and Flemings* [2007]
c_h	Heat capacity of hydrate	2100 ($J K^{-1} kg^{-1}$)	*Liu and Flemings* [2007]
C_i	Seawater salinity	3.5 (wt %)	
c_s	Heat capacity of grains	1381 ($J K^{-1} kg^{-1}$)	*Liu and Flemings* [2007]
c_w	Heat capacity of water	4200 ($J K^{-1} kg^{-1}$)	*Liu and Flemings* [2007]
${D_{l0}}^m$	Diffusion coefficient of methane	10^{-9} ($m^2 s^{-1}$)	*Davie and Buffett* [2001]
${D_{l0}}^s$	Diffusion coefficient of salt	10^{-9} ($m^2 s^{-1}$)	*Davie and Buffett* [2001]
$dT\,dz^{-1}$	The background heat flux resulting in this geothermal gradient for a given thermal conductivity	25 ($mK m^{-1}$)	*Ruppel et al.* [2005b] and *Winters et al.* [2007]
${F_b}^m$	Basal gas flux	1 ($kg m^2 yr^{-1}$)	This study, *Macdonald et al.* [2005], and *Torres et al.* [2004]
g	Gravitational acceleration	9.81 ($m s^{-2}$)	
k	Permeability in absence of hydrate	10^{-12} (m^2)	This study and *Ingebritsen et al.* [2006]
L	Latent heat of hydrate crystallization	421 ($kJ kg^{-1}$)	*Cathles and Chen* [2004]
n_g	Corey exponent (gas)	2	*Bear* [1972] and *Liu and Flemings* [2007]
n_w	Corey exponent (water)	4	*Bear* [1972] and *Liu and Flemings* [2007]
q_g	Gas flux	1, 3, 5 ($kg m^{-2} yr^{-1}$)	*Macdonald et al.* [2005] and *Torres et al.* [2004]
S_{rg}	Irreducible gas saturation	0.02	*Liu and Flemings* [2007] and *Yousif et al.* [1991]
S_{rw}	Irreducible water saturation	0.1	*Liu and Flemings* [2007] and *Yousif et al.* [1991]
T_L	Temperature at base of model	16 (°C)	From T_U and $dT\,dz^{-1}$
T_U	Temperature at seafloor	5 (°C)	*Ruppel et al.* [2005b] and *Winters et al.* [2007]
z_o	Depth below sea level	1070 (m)	This study; Figures 1 and 2
λ_g	Thermal conductivity of methane	0.03 ($W m^{-1} K^{-1}$)	*Sloan* [1998]
λ_h	Thermal conductivity of hydrate	0.5 ($W m^{-1} K^{-1}$)	*Sloan* [1998]
λ_s	Thermal conductivity of grains	1.6 ($W m^{-1} K^{-1}$)	*Class et al.* [2002]
λ_w	Thermal conductivity of water	0.6 ($W m^{-1} K^{-1}$)	*Sloan* [1998]
μ_g	Dynamic viscosity of gas	P and T dependent	*Class et al.* [2002]
μ_w	Dynamic viscosity of water	P and T dependent	*Class et al.* [2002]
ρ_g	Density of methane	P and T dependent	*Duan et al.* [1992]
ρ_h	Density of hydrate	912 ($kg m^{-3}$)	*Sloan* [1998]
ρ_s	Density of grains	2650 ($kg m^{-3}$)	
ρ_w	Density of water	T and salinity dependent	*Duan et al.* [1992]
ϕ	Porosity in absence of hydrate	0.5	Estimated from *Flemings et al.* [2006]
θ^2	Tortuosity	2	Calculated from porosity (ϕ) *Torres et al.* [2004]

model [*Liu and Flemings*, 2007]. This pore-filling model is in agreement with the recovery of hydrate disseminated within fine-grained sediments at Ursa [*Winters et al.*, 2007]. We use the J-function to model capillary pressure, and we calculate relative permeabilities with Corey's model [*Bear*, 1972; *Liu and Flemings*, 2007]. Fluid density and viscosity are a function of salinity, temperature, and pressure [*Class et al.*, 2002; *Duan et al.*, 1992; *Liu and Flemings*, 2007]. Permeability, porosity, relative permeability, and capillary pressure are a function of hydrate saturation as discussed in *Liu and Flemings* [2007] (Table 2).

3.2. Model Simulation

We model the pressure and temperature conditions of those at the Ursa vent (Table 2 and Figure 4). We assume constant temperature at the seafloor (5°C) and at the base of the model (16°C at 440 mbsf). The basal temperature boundary condition is calculated from the measured seafloor temperature and the background geothermal gradient of 25 mK m^{-1} [*Ruppel et al.*, 2005b]. We assume sediment permeability in the absence of hydrate is 10^{-12} m^2. This permeability is typical of sand in the shallow crust [*Fetter*, 1994]. Initial porosity and salinity are assumed to be constant throughout the model column at 0.5 and 3.5 wt %, respectively [*Flemings et al.*, 2006]. This porosity is an approximate average for sediments adjacent to the vent in the Ursa basin at depths >20 mbsf [*Flemings et al.*, 2006].

We use a grid spacing of 20 m for the finite-difference scheme. The basal gas flux is 1 kg m^{-2} yr^{-1}. Field data suggest that a typical GoM vent releases gas at a rate of $\sim 2.2 \times 10^5$ kg yr^{-1} [*Macdonald et al.*, 2005], although the exact area over which this seepage occurs is not well constrained. At Ursa, the vent edifice is approximately 1 km in diameter, and the negative-polarity event at the seafloor is approximately 200 m wide (Figure 1). If the gas release is assumed constant over the area of a circular vent with a diameter of

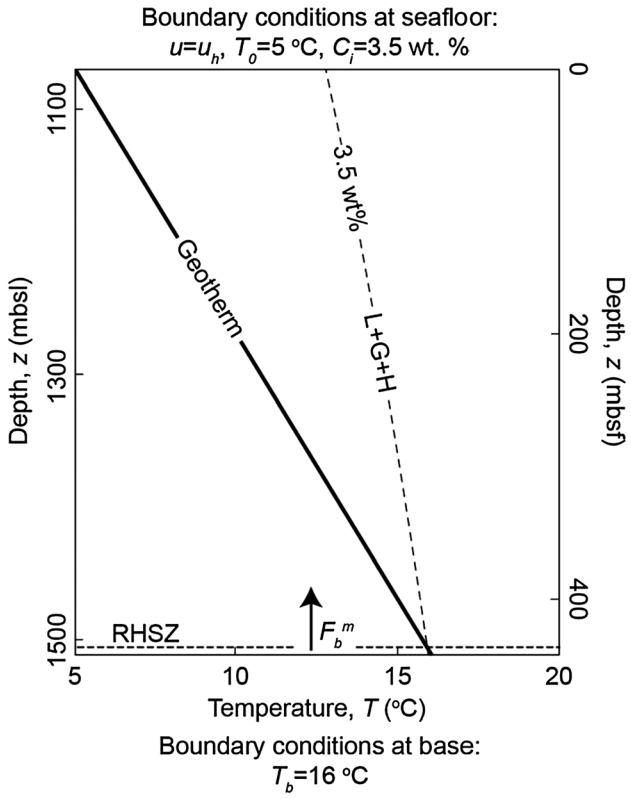

Figure 4. Initial and boundary conditions for the dynamic model. The intersection of the three-phase hydrate equilibrium curve (thin dashed line) with the geothermal gradient (solid black line) defines the base of the RHSZ (horizontal dashed line). Initially, the model is hydrostatically pressured ($u = u_h$), water has seawater salinity ($C = C_i = 3.5$ wt %), and there is no methane present ($X_l^m = S_v = S_h = 0$). There are constant-temperature boundary conditions at the seafloor ($T_o = 5$°C) and the base of the model ($T_b = 16$°C), determined by the background geothermal gradient of 25 mK m^{-1} [*Ruppel et al.*, 2005b]. Pressure, salinity, methane concentration, and gas and hydrate saturation are set as constant at the seafloor ($u = u_h$, $C = C_i$, $X_l^m = S_v = S_h = 0$). A basal methane flux (F_b^m) of 1 kg m^{-2} yr^{-1} is supplied from below.

200–1000 m, then the range of gas fluxes from GoM vents is 0.28–7.1 kg m^{-2} yr^{-1}. We select 1 kg m^{-2} yr^{-1} since this is in agreement with gas flux estimates observed at other venting locations [*Tréhu et al.*, 2004] and since this value has been used in previous modeling studies [*Liu and Flemings*, 2006, 2007].

3.2.1. Propagation of the Reaction Front

As dissolved methane gas fluxes into the base of the model column at the rate it is supplied, the dissolved methane concentration exceeds its $l + g$ solubility, and free-gas bubbles form (Figure 5d). This free-gas migrates into the RHSZ and combines with water to form hydrate. A three-phase zone develops within the RHSZ, in which free gas, dissolved methane, and hydrate coexist (Figures 5c–5e). Beneath this three-phase zone, methane pore water concentration is maintained at its maximum $l + g$ solubility, and above this zone, methane concentration is below its maximum $l + h$ solubility (Figure 5e) [*Liu and Flemings*, 2006].

As hydrate forms, salt is excluded and heat is released, resulting in the generation of warm, saline pore water. At a given depth, hydrate formation continues until pore water is too warm and too salty for further hydrate formation. This process self generates a three-phase ($l + g + h$) reaction front that propagates toward the seafloor with time (Figure 5). The initial pressure and temperature near the seafloor result in conditions that are furthest into the $l + h$ stability zone and furthest from three-phase stability (Figure 3d). Therefore, pore water at shallower depths needs to be successively saltier and warmer, and hydrate saturations higher in order to create three-phase stability (Figures 5a–5c). This results in an upward increase in salinity and hydrate saturation (Figures 5b and 5c). Temperatures decrease toward the seafloor but are elevated higher than the background geothermal gradient at increasingly shallow depths (Figure 5a). Since more hydrate needs to form closer to the seafloor to elevate salinity and temperature to three-phase equilibrium, the propagation rate of the reaction front decreases with time (Figure 5).

The seafloor heating from the advancing reaction front first occurs at ~1000 years (kyr). Temperature is assumed constant (5°C) at the seafloor; and as a result, a large temperature gradient develops below the seafloor (Figure 5a). The temperature gradient between the seafloor and the first grid block below the seafloor (20 mbsf) increases with time to a maximum of 114 mK m^{-1} at 8 kyr (Figure 5a). This temperature gradient is produced just before breaching of the reaction front at the seafloor (~10 kyr) and occurs when hydrate saturations near the seafloor are increasing most rapidly (Figure 5c). After breaching, hydrate-formation rates slow, and temperatures within the RHSZ cool due to upward heat transport along the temperature gradient below the seafloor.

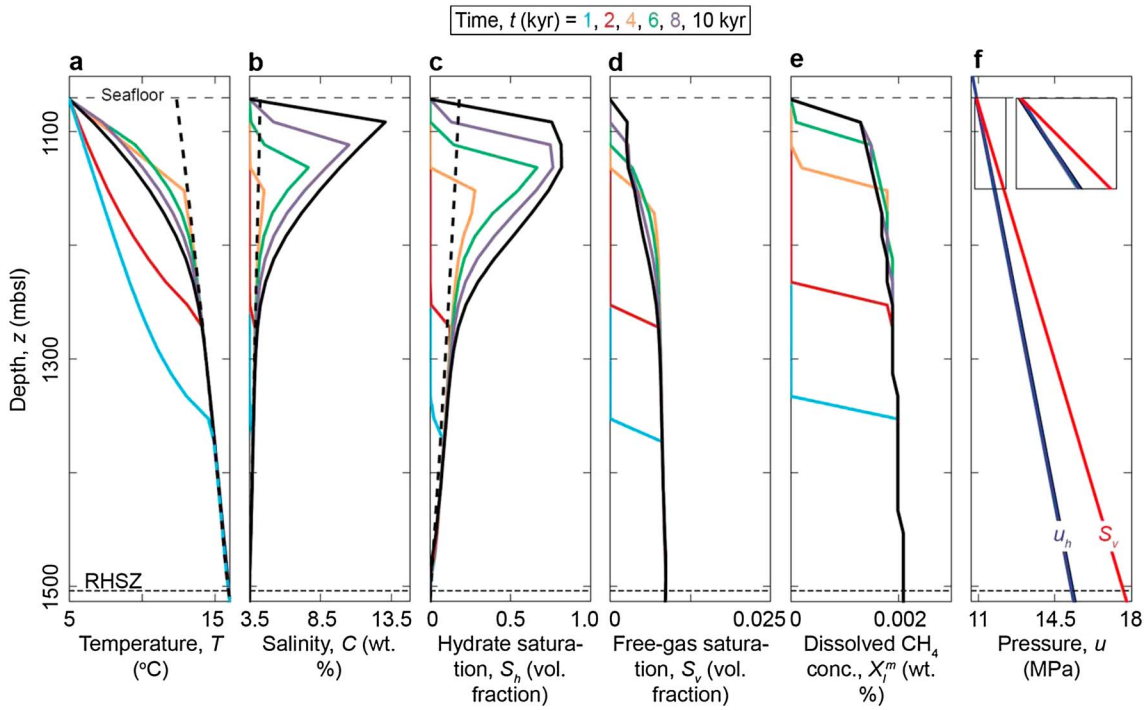

Figure 5. Propagation of reaction front toward the seafloor and temporal evolution of (a) temperature, (b) salinity, (c) hydrate saturation, (d) free-gas saturation, (e) methane concentration, and (f) water pressure at 1 (blue), 2 (red), 4 (orange), 6 (green), 8 (purple), and 10 (black) thousand years (kyr). Figure 5f shows the hydrostatic stress gradient ($u_h z^{-1}$, dark blue line) and lithostatic-stress gradient ($S_v z^{-1}$, red line). At ~10 kyr, the reaction front breaches the seafloor. Thereafter, free gas vents from the base of the RHSZ to the seafloor. Dotted black line shows simulated temperature, salinity, and hydrate saturation for the closed-system model (Figure 3).

Initially, temperature, salinity, and hydrate formation follow those predicted by the insulated equilibrium model (Figures 5a–5c). But as the reaction front advances toward the seafloor, the elevated temperature gradient below the seafloor prompts enhanced vertical heat flow from the reaction front to the seafloor (Figure 5a). The reaction front also generates two salinity gradients. One gradient exists between the reaction front and the seafloor, and the other gradient exists between the reaction front and the base of the RHSZ (Figure 5b). These salinity gradients cause salt to diffuse upward and downward from the reaction front. To replace this heat and salt loss, hydrate formation continues within the RHSZ even after the reaction front has propagated further (Figure 5c). However, due to the efficiency of thermal conduction as a heat-transport process (~10^{-6} m^2 s^{-1}) compared to chemical diffusion as a salt-transport process (~10^{-9} m^2 s^{-1}) [*Rempel and Buffett*, 1997], heat is drawn away from the reaction front more rapidly than salt. This causes sediments below the reaction front to become cooler and saltier over time (Figures 5a and 5b). As a result, after ~4 kyr, simulated salinity and temperature begin to deviate significantly from the closed-system model (Figures 5a–5c and Movie S1 in the supporting information).

During propagation, there is substantial, but variable, water discharge at the seafloor (1.8–3.2 kg m^{-2} yr^{-1}) (Figure 6a). These fluxes are driven by volume expansion during hydrate formation (~10%) at and below the reaction front. After breaching (~10 kyr), these fluxes decrease to less than 1.2 kg m^{-2} yr^{-1} because the rate of hydrate formation within the RHSZ also diminishes. Below the reaction front, gas flux is maintained approximately at values at which it is supplied from below; and above the front, gas fluxes are zero (Figure 6b). Gas is first expelled at the seafloor once breaching occurs (Figure 6b).

3.2.2. Postbreaching Behavior and Dissipation

After the three-phase reaction front breaches the seafloor (~10 kyr), free gas flows from the base of the RHSZ into the ocean (Figure 8b). Initially, the mass flux of methane released at the seafloor is 2 to 3 times smaller than the flux supplied at the base of the model (Figure 8). This is because hydrate continues to accumulate within the RHSZ, particularly between 1200 and 1350 mbsl, as heat and salt are lost from the system (Figure 7). Because the conduction of heat out of the system outpaces the diffusion of salt, temperatures within the RHSZ cool over time; as a consequence, salinities increase as additional hydrate forms until three-phase equilibrium is achieved (Figures 7a and 7b). This continued hydrate formation causes volume expansion that drives water fluxes toward the seafloor (Figure 8a).

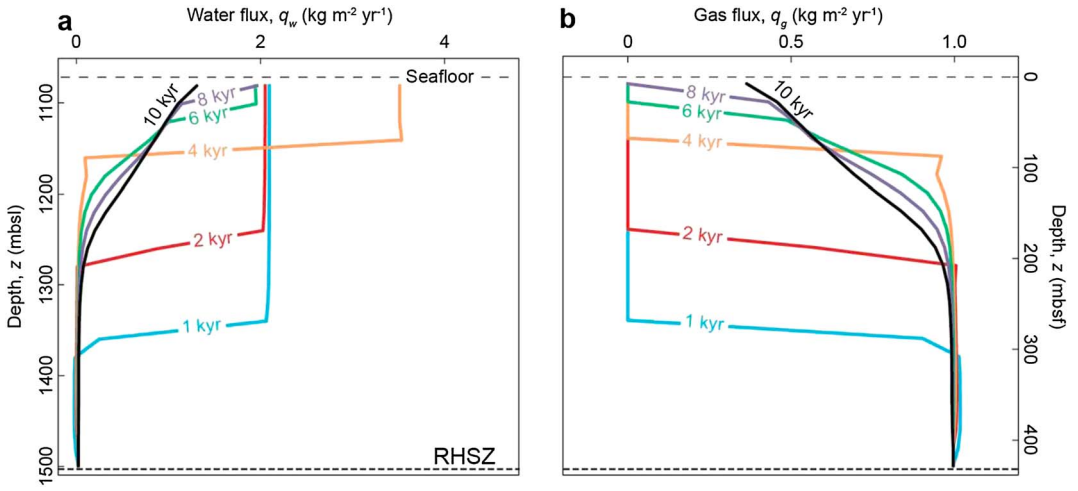

Figure 6. (a) Water and (b) gas fluxes as functions of depth and time. Fluxes are correlative with simulations in Figure 5. Fluxes are calculated every 20 m (block spacing) at block interfaces instead of at block centers. For this reason, flux is not calculated at the seafloor (1070 mbsl) but 10 mbsf (1080 mbsl). Gas fluxes are cumulative advective and diffusive methane fluxes.

Just after breaching (10 kyr), the highest salinity value is at the first grid block below the seafloor, and yet the highest hydrate saturation is at the second grid block below the seafloor (Figures 7b and 7c). However, with time, hydrate saturations within the first grid block increase to values greater than saturations anywhere else within the model domain (Figure 7c). Because a constant seawater salinity is assumed at the seafloor, a sharp salinity gradient develops between the seafloor and the first grid block below the seafloor (Figure 7b). Salt is

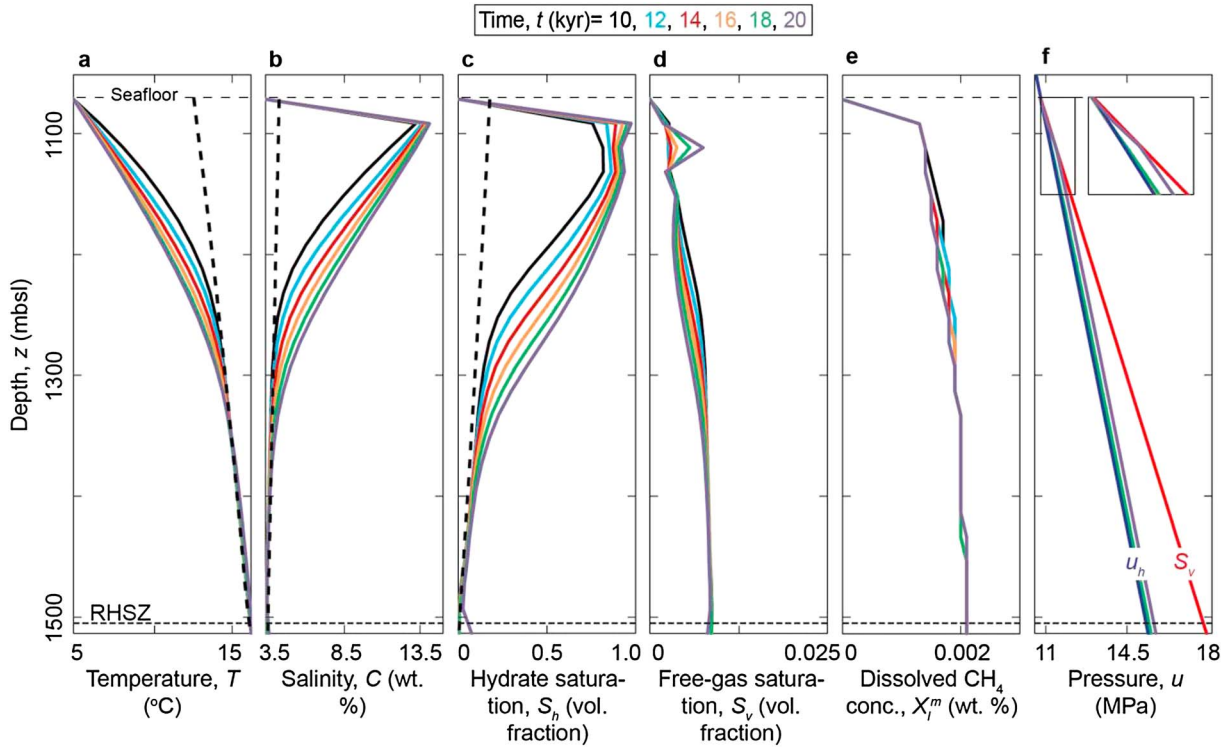

Figure 7. (a–f) Postbreaching behavior of vent at 10 (black), 12 (blue), 14 (red), 16 (orange), 18 (green), and 20 (purple) kyr. After breaching (when gas enters the ocean at ~10 kyr), hydrate continues to form throughout the model domain due to the vertical diffusion and conduction of salt and heat, respectively. Heat flow via conduction outpaces chemical transport via diffusion. Therefore, temperatures diminish over time, and salinity increases. At 20 kyr, water pressures 40 mbsf exceed the lithostatic stress. Thereafter, water pressures may dilate fractures and push fluids through the HSZ to the seafloor.

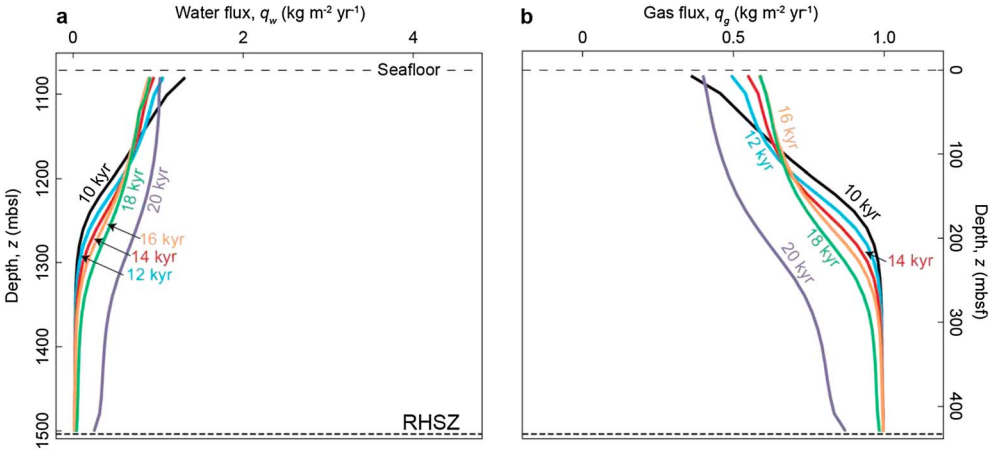

Figure 8. (a) Water and (b) gas fluxes after breaching. Fluxes are correlative with simulations in Figure 7. Water fluxes are present due to volume expansion from hydrate solidification. Gas fluxes decrease toward the seafloor because gas crystallizes as hydrate. At 20 kyr, hydrate forms at the base of the model due to the generation of elevated pore pressures which make hydrate stable at depths below the RHSZ.

transported toward the seafloor along this gradient by chemical diffusion. This loss of salt drives continued rapid hydrate formation: with abundant gas supply, hydrate continually forms in proportion to the amount of salt lost.

3.2.3. Postbreaching Steady State Behavior

After breaching, the simulated salinity and temperature near the seafloor asymptotically approach a fixed value of approximately 0.55 wt % m^{-1} and 28.5 mK m^{-1} (Figure 9). This is most clearly illustrated with the 1 kg m^{-2} yr^{-1} simulation, which ran for the longest time (Figure 9). The salinity gradient evolves to equal that necessary to ensure three-phase equilibrium at the first grid block beneath the seafloor. In turn, the thermal gradient evolves to transport any heat generated by ongoing hydrate formation. In Appendix A, we assume conservation of mass of the salt and calculate the amount of hydrate formed due to salt diffusion to the seafloor and due to an influx of water. The mass of hydrate added per unit time over the entire zone where hydrate is formed is

$$\int_0^{Z_{HSZ}} \frac{dS_h}{dt} dz = \frac{X_h}{dt} = \frac{\rho_h \phi D_{l0}^s a}{\theta^2 C_{eq}} + \rho_h \frac{q_w}{\phi} \ln\left[\frac{C_{eq}}{C_i}\right]. \quad (11)$$

Z_{HSZ} is the thickness of the regional hydrate stability zone (435 m), C_i is the seawater salinity (3.5%), C_{eq} is the equilibrium (triple-point) salinity at the seafloor, ϕ is the porosity (0.5), θ^2 is the tortuosity (2), $D_{l0}{}^s$ is the diffusion coefficient of salt (10^{-9} m^2 s^{-1}), ρ_h is the density of hydrate, X_h is the mass of hydrate, q_w is the Darcy velocity, and a is the salinity gradient within the diffusive boundary layer caused by seafloor salinity at the seafloor and triple-point conditions immediately beneath the seafloor. In the numerical model, the depth to the triple-point condition is the distance to the first grid block beneath the seafloor. The first term in equation (11) describes the amount of hydrate formed due to diffusion of salt from the triple-point conditions beneath the seafloor upward to the seafloor. The second term describes the amount of hydrate formed due to flow of water into the hydrate stability zone (HSZ). In this case, water of seawater salinity supplied from below freshens the more saline pore waters within the RHSZ. In both cases, salinity is decreased in the system and in response, gas that is present forms additional hydrate until a new three-phase equilibrium is achieved.

The steady state temperature gradient ($dT\,dz^{-1}$) necessary to remove the heat by conduction that is created by the hydrate formation is

$$\frac{dT}{dz} = \frac{Q_e + \frac{\rho_h \phi D_{l0}^s a L}{\theta^2 C_{eq}} + \rho_h \frac{q_w}{\phi} \ln\left[\frac{C_{eq}}{C_i}\right] L}{\lambda}. \quad (12)$$

Q_e is the heat flux provided at the base of the model (25 m W m^{-2}), L is the latent heat of hydrate formation (421 kJ kg^{-1}), and λ is thermal conductivity (1 W m^{-1} K^{-1}).

We use equations (11) and (12) to calculate the steady state salinity and temperature gradients that our numerical model should converge to assuming only gas flow and a 20 m grid spacing. We start with the

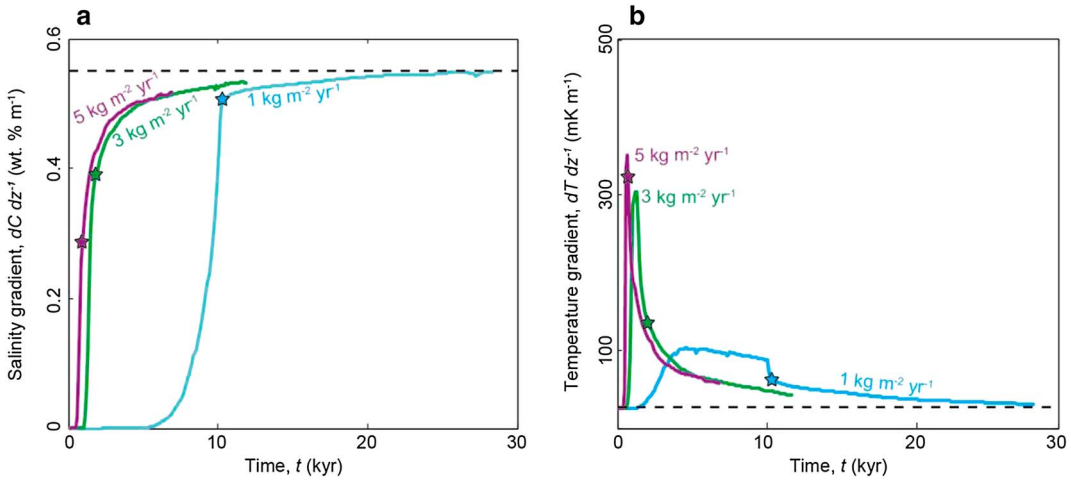

Figure 9. Temporal evolution of simulated salinity gradients and temperature gradients between the seafloor and the first grid block below seafloor for the 1, 3, and 5 kg m^{-2} yr^{-1} gas fluxes. (a) Salinity gradients increase over time for each simulation. The greater the gas flux, the faster the propagation rate of the reaction front. Stars indicate when breaching occurs. Water pressures exceed the lithostatic stress after 20, 3.5, and 2.8 kyr for the 1, 3, and 5 kg m^{-2} yr^{-1} gas fluxes, respectively. We continue to run the simulation with these elevated water pressures to elucidate steady state behavior. For each gas flux, the subseafloor salinity gradient approaches a steady state profile (horizontal dashed line, 0.55 wt % m^{-1}). (b) Temperature gradients increase to maximum values just before breaching occurs. Thereafter, they relax to steady state values. Temperature gradients ultimately approach steady state values (horizontal dashed line, 28.5 mK m^{-1}).

background heat flux (Q_e) and then solve for the equilibrium salinity at 20 mbsf and then use this equilibrium salinity to determine the hydrate-saturation change from equation (11). Then, we update the temperature gradient (dT dz^{-1}) according to equation (12) and iterate until all dependent variables (C_{eq}, dT dz^{-1}) converge with a relative error less than 10^{-4}.

For the example with no water flow and a 20 m grid spacing, we find that the steady state temperature gradient is 28.5 mK m^{-1} and the equilibrium salinity at 20 m depth is 14.6 wt %. This results in a steady state salinity gradient of 0.55 wt % m^{-1}. The background temperature gradient is 25 mK m^{-1}; thus, hydrate formation contributes 3.5 mK m^{-1} to the heat flow or an additional 14% relative to the background thermal gradient (Figures 9 and 10). These values are delineated with horizontal dashed lines on Figure 9. The simulation results for a 1 kg m^{-2} yr^{-1} gas flux reach these values. Simulations for higher gas fluxes (3 and 5 kg m^{-2} yr^{-1}) approach these values but were stopped before steady state was reached.

Figure 9 illustrates an important aspect of the numerical model: the grid spacing controls the magnitude of salt diffusion at the upper boundary. As grid spacing is decreased, the seafloor salinity and temperature gradients increase sharply (Figure 10a). This is because the salinity at the grid block beneath the seafloor always equals the salinity necessary for three-phase equilibrium and because the seafloor salinity is fixed. The increase in salinity gradient with decreased grid spacing results in increased salt transport by diffusion, which induces hydrate formation and hence a higher temperature gradient caused by the heat of formation of the hydrate. Although the gradients increase, the ratio of the gradients is independent of grid size (Figure 10b). For example, with no water flux, the ratio of the deviation in the temperature gradient (3.5 mK m^{-1}) to the salinity gradient (0.55 wt % m^{-1}) is approximately 6 (3.5/0.55) (Figure 10b). With water flow, the ratio increases with increasing grid size (Figure 10b). This is because the salinity gradient decreases as the grid spacing increases; however, the deviation in the temperature gradient remains high from hydrate formation produced via the upward flow of relatively fresh water into the RHSZ.

3.2.4. The Effect of Increasing Gas Flux

We explore how higher gas fluxes (3 and 5 kg m^{-2} yr^{-1}) affect the simulated salinity and temperature during the formation of a gas chimney. The simulations are identical except for the higher basal gas flux. As in the previous simulation, distinct phases of propagation, dissipation, and hydrate sealing occur (Figure 9). However, the higher gas flux creates significantly higher hydrate-formation rates during propagation and dissipation. These higher hydrate-formation rates result in a faster propagation of the reaction front toward

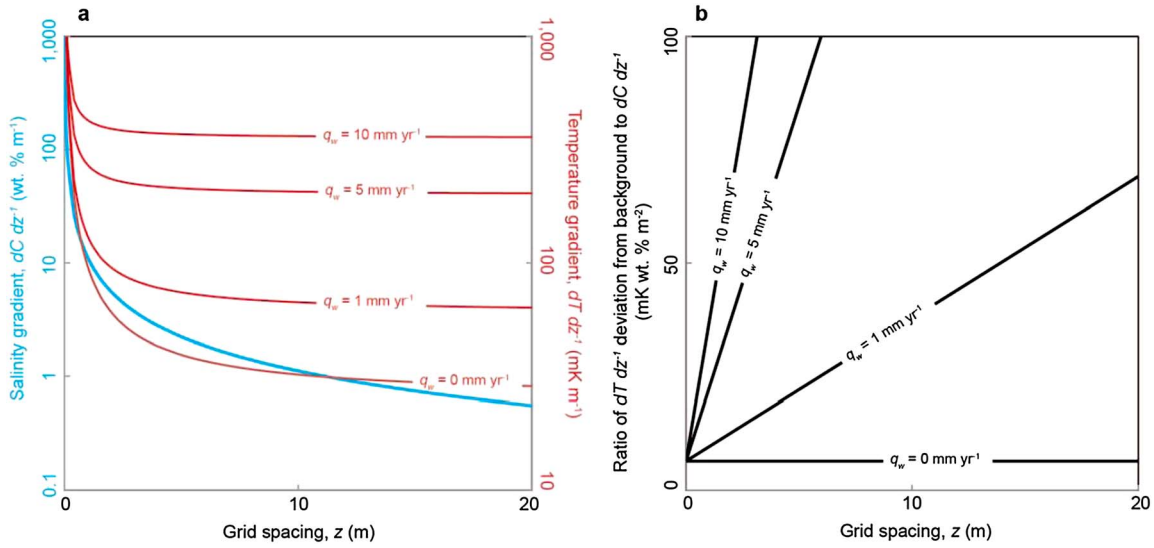

Figure 10. (a) Late-stage steady state salinity gradient ($C_{eq} - C_i)/\Delta z$ versus grid spacing (blue line) and modeled temperature gradient versus grid spacing for water fluxes of 0, 1, 5, and 10 mm yr^{-1} (red line; equations (11) and (12)). The greater the water flux, the higher the simulated temperature gradient for a given grid spacing. (b) The ratio of deviation from the background temperature gradient ($dT\,dz^{-1} - 25$ mK m^{-1}) to the salinity gradient for a range of grid sizes. For a given grid spacing, the deviation from the background temperature gradient is larger than the salinity gradient by a factor of ~6 if no water flux is present. If a water flux is present, then the ratio of the deviation from the background temperature gradient to the salinity gradient increases with increasing grid size. This is because the salinity gradient decreases as the grid spacing increases. However, because water flow is present, high-temperature gradients are still produced from hydrate formation via the upward flow of relatively fresh waters into the RHSZ.

the seafloor. For the 3 and 5 kg m^{-2} yr^{-1} gases, breaching occurs after 2 and 0.8 kyr, respectively, compared to 10 kyr for the 1 kg m^{-2} yr^{-1} case (Figure 9).

During propagation, the higher basal gas fluxes generate temperature gradients between the seafloor and the first grid block below the seafloor that are significantly elevated compared to the 1 kg m^{-2} yr^{-1} gas flux. Simulated temperature gradients reach a maximum of 309 and 352 mK m^{-1} for the 3 and 5 kg m^{-2} yr^{-1} gas fluxes just before breaching (Figure 9a). After breaching, hydrate-formation rates diminish, and the conduction of heat away from the chimney outpaces the diffusion of salt. This causes temperature gradients to gradually relax to steady state values (28.5 mK m^{-1}) and salinity gradients to increase so that equilibrium salinity for the steady state temperature gradient (14.6 wt %) is present at the first grid block below the seafloor (Figure 9). Eventually, steady state behavior is reached as described in equations (11) and (12).

For the 1 kg m^{-2} yr^{-1} gas flux, the simulated salinity and temperature gradients clearly approach these steady state values (Figure 9). For the higher gas fluxes, hydrate sealing and overpressure generation occur before this steady state can be reached. However, we suggest that at long timescales, the temperature gradient will approach the steady state value, and the salinity gradient will increase so that equilibrium salinity, given the steady temperature gradient, is present at the first grid block below the seafloor.

3.2.5. Hydrate Sealing and Overpressure Generation

Eventually, all pore space at the first grid block below the seafloor will fill with hydrate, which will block flow. As hydrate fills the pore space at the first grid block below the seafloor, the pore-throat diameter decreases, causing permeability reduction [*Kleinberg et al.*, 2003; *Liu and Flemings*, 2007]. Volume expansion from hydrate formation tries to push water through the reduced pore-throat size; the water cannot escape fast enough; and as a result, water pressure rises (Figure 7f). Eventually, water pressures are generated that exceed the lithostatic stress at the second grid block below the seafloor (Figure 7f). These elevated pressures cause hydrate solidification at depths below the RHSZ (Figure 7c). Hereafter, elevated pore pressures may dilate fractures and push fluid (gas and water) through the HSZ. We do not simulate this behavior with this model. The timescale over which this occurs is dependent on the size of the upper grid block and on fluid fluxes. For the 20 m grid size that we assume, this stage is reached after ~20, 3.5, and 2.8 kyr for the 1, 3, and 5 kg m^{-2} yr^{-1} gas fluxes, respectively.

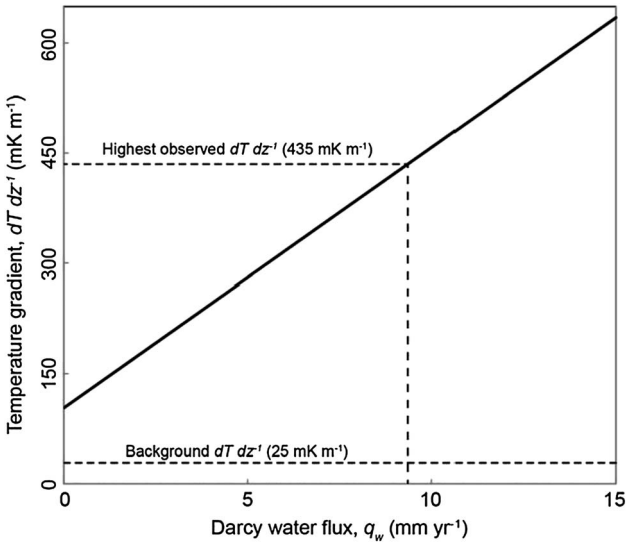

Figure 11. The steady state temperature gradient that results for a range of Darcy water fluxes at the Ursa vent. Figure assumes that gas is always supplied in excess of its proportion in hydrate and that the steady state salinity gradient is 11.9 wt % m^{-1} (PC-25, Figure 1b). Horizontal dashed black lines show highest observed temperature gradient at the Ursa vent (435 mK m^{-1}) and the background geothermal gradient (25 mK m^{-1}). A water flux of ~9.5 mm yr^{-1} must accompany an upward gas flux to simulate the highest observed temperature gradient.

4. Application to the Ursa Vent, Northern Gulf of Mexico

The piston core taken closest to the center of the vent (PC-25) (Figure 1) records a seafloor salinity gradient of 11.9 wt % m^{-1} if seawater salinity (3.5 wt %) is assumed at the seafloor. The temperature gradient at the vent is 435 mK m^{-1} at TM 5–9 and 301 mK m^{-1} at TM 5–8. Assuming the salinity gradient is 11.9 wt % m^{-1} and the temperature gradient is 435 mK m^{-1}, three-phase stability lies at ~1 mbsf for a pure methane system (using the thermodynamic model of *Duan et al*. [1992] and *Henry et al*. [1999]). Our result is slightly different than *Ruppel et al*.'s [2005b] calculated depth of 5.7 mbsf because they use a different hydrate stability model, Colorado School of Mines Hydrate program [*Sloan*, 1998], and because they assume salinity remains constant below the deepest measured value. The background temperature gradient at Ursa is 25 mK m^{-1}. Thus, the deviation from the background thermal gradient is 410 mK m^{-1} (435 mK m^{-1}–25 mK m^{-1}) and the ratio of deviation from background heat flux to salinity gradient is 34.4 (410/11.9). This is approximately 5 times greater than the simulated examples and implies that significant water flux is present.

We interpret that the Ursa vent is a long-lived feature and that it is currently in its final, steady state phase. We use equations (11) and (12) to quantify the water flux necessary to reconcile the observed temperature and salinity profiles. We first calculate that, given the observed salinity gradient of 11.9 wt % m^{-1} and no water flow ($q_w = 0$), the temperature gradient should be approximately 100 mK m^{-1}° (Figure 11). This is much lower than the observed temperature gradient of 435 mK m^{-1}. We then calculate (equation (12)) that a Darcy flux of 9.5 mm yr^{-1} is necessary in order for the simulated temperature gradient to equal the observed (equation (12)). This extra water freshens the system and forces hydrate to form which elevates the temperature gradient (Figure 11). We also note that this provides a limiting value for the gas flux that must be present. In order for methane to be supplied equal to its proportion in hydrate (~13.4% by mass), then a gas flux of at least ~1.3 kg m^{-2} yr^{-1} must be present for this water flow.

5. Discussion

We envision that a hydrate system fed from below by gas undergoes three distinct phases (Figure 12). First, a free-gas/hydrate reaction front propagates toward the seafloor and elevates salinity and temperature to three-phase equilibrium at the reaction front (Figure 12a). In this stage, the release of heat from hydrate formation is significantly more important in shifting hydrate stability conditions than the exclusion of salt. As a result, subseabed temperature gradients are highest during this stage and reach a maximum just before the reaction front breaches the seafloor.

Second, after breaching, elevated salinities and temperatures dissipate away from the three-phase chimney. Because heat conduction outpaces chemical diffusion, pore water within the gas chimney becomes cooler and saltier over time (Figures 12b and 12c). Continued hydrate formation during dissipation results in permeability reduction, which traps water and elevates water pressures to values that exceed the total vertical stress. Hereafter, pore pressures likely fracture the overburden, increasing permeability, and allowing gas and water to flow through the RHSZ to the seafloor. We note that in a two or three-dimensional model,

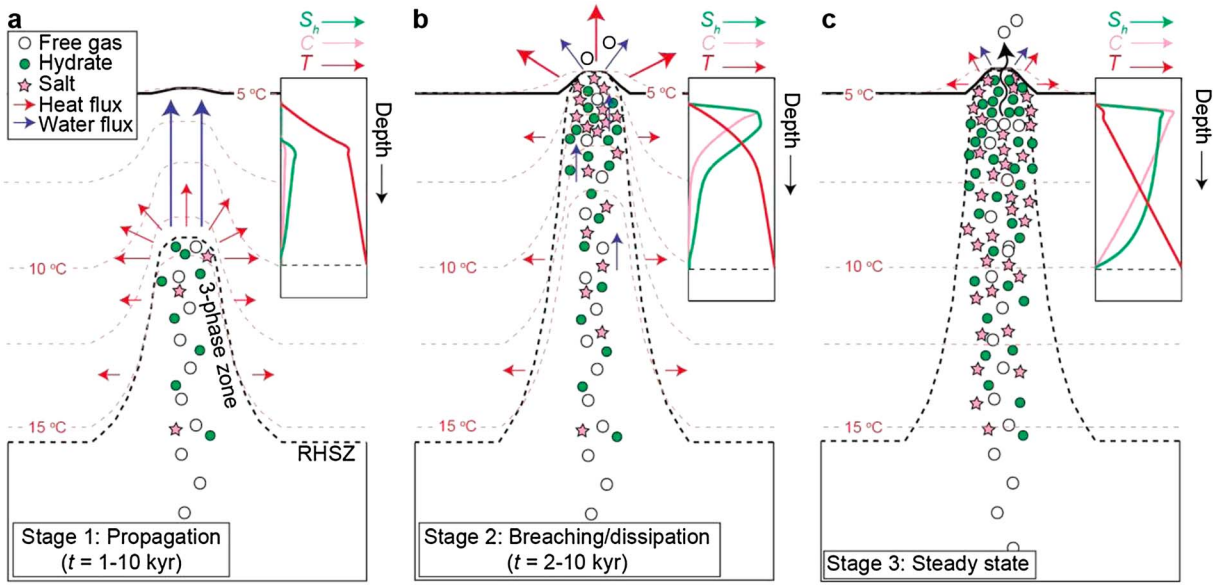

Figure 12. Evolution of the venting system. (a) Free gas (white circles) is supplied from below; when this gas reaches the base of the RHSZ, gas and water combine to form hydrate (green circles). Salt (pink stars) is excluded during this process, and heat is released. Hydrate formation continues until the pore water is too warm and salty for further hydrate formation. Hydrate formation self generates three-phase hydrate equilibrium from the base of the RHSZ to the seafloor. This process lasts between 1 and 10 kyr, depending on the basal gas flux. (b) Once the hydrate reaction front breaches the seafloor, hydrate formation continues at a rate necessary to replace the loss of salt and heat from diffusion and conduction, respectively. The conduction of heat away from the chimney outpaces the diffusion of salt. As a result, the chimney becomes saltier and cooler over time. (c) Continued hydrate formation just below the seafloor results in permeability reduction, which causes water pressures to exceed the vertical stress. Hereafter, fracturing (black arrow) may occur, and water pressures will push fluids through the HSZ. Eventually, a steady state is reached in which temperatures in the chimney relax to background values, and salinities increase to values necessary for three-phase equilibrium given the background thermal gradient. In this steady state, hydrate formation only occurs directly below the seafloor, and it occurs at a rate necessary to replace diffuse salt loss. This steady state hydrate formation has the potential to produce large, steady fluxes of salt and heat to the ocean.

it is possible that hydrate formation and pore-throat reduction may encourage lateral gas migration and the propagation of more tortuous escape pathways. In fact, recent observations at a free-gas/gas-hydrate system offshore SW Africa indicate that hydrate formation may cause reduction in vertical sediment permeability and the redirection of rising fluids to surrounding sediments [*Marcon et al.*, 2014]. Future modeling efforts in two and three dimensions must be done to better understand the importance of these processes.

Eventually, the temperature gradient within the RHSZ relaxes toward a steady state value where heat loss balances the heat generated due to hydrate formation, and the hydrate formation is controlled by the rate of salt loss. This continued hydrate formation produces steady and significant salt and heat fluxes to the ocean (Figure 12c and Movie S1). We have specifically developed an approach to estimate the water flux necessary to create a particular salinity and thermal gradient.

Our model suggests that the coexistence of high salinities, high-temperature gradients, gas hydrate, and free-gas expulsion at Ursa and other vents around the world, can be explained as the natural result of gas migration through the hydrate stability zone. We further interpret that many long-lived vent systems may be at steady state: elevated temperature and salinity gradients are maintained by the continuous solidification of hydrate near the seafloor. At these systems, gas hydrate coexists with seafloor gas expulsion and high salinities/temperatures that shift the vent to three-phase equilibrium [*Hornbach et al.*, 2005; *Liu and Flemings*, 2006; *Milkov et al.*, 2004; *Pape et al.*, 2011; *Römer et al.*, 2012; *Ruppel et al.*, 2005b; *Sahling et al.*, 2009]. As excess gas supplied from below bubbles through to the ocean, hydrate forms at or near the seafloor and is limited by the rate that salt escapes. Each vent is its own thermal reactor that is fueled by a gas-to-hydrate phase change near the seafloor. This hydrate formation likely drives the creation of mounts of hydrate at the seafloor and in the subsurface that have been observed in the Santa Monica Basin, offshore California [*Paull et al.*, 2008] (Figure 11). In addition, this hydrate formation produces a steady heat flow which drives the extraordinarily high-temperature gradients that have been observed at venting locations around the world [e.g., *Pape et al.*, 2011; *Ruppel et al.*, 2005b; *Sahling et al.*, 2009]. To explain the observations at Ursa, we estimate that there is a Darcy aqueous flux of 9.5 mm yr^{-1} and that there is a gas flux that is no less than 1.3 kg m^{-2} yr^{-1}.

The model presented here is an alternative to that presented by *Smith et al*. [2014]. In that model, *Smith et al*. [2014] showed that the observed temperature and salinity gradients at Ursa could be explained by deeply sourced salty water flowing upward at 30 mm yr^{-1} and hydrocarbon flowing upward at 41–190 kg m^{-2} yr^{-1}. While the model of *Smith et al*. [2014] reconciles the observed temperature and salinity gradients, it requires a very high-hydrocarbon flux to account for the high-temperature gradient present. This hydrocarbon flux is significantly greater than previous estimates.

The two model approaches represent end members of the hydrogeological processes present at deepwater vents, and these models are distinct and testable. For example, in the hydrate solidification model, the salinity present near the seafloor is the triple-point salinity. Thus, if the hydrate solidification is the driving process then the seafloor salinity should always be at the triple point and vents in the deeper water should record higher salinities than vents in shallower water because the deeper water is further from equilibrium. Second, high salinities present in vent systems without any obvious source of salt can only result from the hydrocarbon-solidification model presented here. Third, geochemical measurements such as Na^+ to Cl^- ratios and strontium isotopes will help to distinguish deep advection and hydrate solidification as heat- and salt-generating processes [*Reitz et al*., 2007]. For example, if high-salinity fluids are derived from hydrate solidification, then the Na^+ to Cl^- ratios will be close to that of seawater (~0.85), whereas if high-salinity fluids are derived from subsurface salt bodies, then the ratio will be closer to that of halite (1.0). $^{87}Sr/^{86}Sr$ values can further clarify whether brine-enriched fluids are sourced from depth or generated via shallower processes like hydrate solidification [*Reitz et al*., 2007]. Finally, modeling studies in two and three dimensions will help to reconcile the apparent discrepancy between measured geochemical and temperature data at vents. For example, the mismatch in aqueous flow rates necessary to explain the salinity and temperature data in the model of *Smith et al*. [2014] may simply be due to the limited ability to target vents using shipboard coring devices versus submersible push cores as well as differences in chemical versus thermal diffusivity. Future field and modeling studies will illuminate which of these processes are driving the presence of high salinities, high temperatures, and hydrate venting at deepwater vents around the world.

5.1. Model Limitations

Our model is one-dimensional and we recognize that both heat and salt may diffuse laterally away from the salty three-phase gas chimney to the surrounding normal salinity pore water. In previous work, we have shown that a vertical gas flux of ~1 kg m^{-2} yr^{-1} far exceeds the rate of gas depletion due to continued hydrate formation caused by lateral diffusion of salt [*Liu and Flemings*, 2006, 2007]. This indicates that even in a two-dimensional model, the lateral diffusion of salt will not outpace gas supply from below and that therefore a gas chimney will form and be maintained. Salinity and temperature will be maintained at three-phase equilibrium by continued hydrate formation even though salt is transported away laterally. Thus, a one-dimensional model is a reasonable approximation of two-dimensional behavior in a gas chimney.

We assume that gas is 100% methane, even though gas from hydrates recovered at Ursa reveals the presence of heavier hydrocarbon gases (75.2% C_1, 7.5% C_2, 11.2% C_3, 5.5% i-C_4, and 0.5% n-C_4) [*Sassen et al*., 2001]. This different gas composition affects the depth of the RHSZ by tens of meters and would result in salinity and/or temperature needing to be even greater within the vent to generate three-phase equilibrium [*Sloan*, 1998]. We also assume that gas is supplied from depth at a constant rate, even though flow from GoM vents varies significantly in time and space [*Hu et al*., 2012; *MacDonald et al*., 2000]. All of these factors would contribute to the precise water flux necessary to explain the observed temperature and salinity profiles. However, it would not change the fundamental insights gained through the model.

The assumption of constant salinity and constant temperature at the seafloor is a simplification of the physical behavior at the ocean-seafloor interface. For example, as salt diffuses to the seafloor with a high concentration, we would expect a boundary layer to build up with concentrated salt in the water column [*Fer and Haugan*, 2003; *McDougall*, 1984; *Turner and Gustafson*, 1978]. In fact, such dense, saline ponds have been observed on the seafloor at Ursa and other deepwater GoM vents [*MacDonald et al*., 2003]. This boundary layer might limit diffusive salt transport [*Fer and Haugan*, 2003] and if so an even higher water flux would be required. Similarly, but perhaps less significantly, it is possible that a thermal boundary layer would develop that would limit heat transport. Future work will address refining this boundary condition.

6. Conclusions

Gas vents that pierce the HSZ and transport free methane gas from depth into the ocean are ubiquitous components of the world's oceans. We present a one-dimensional model that couples the thermodynamics of hydrate solidification with multiphase flow to illuminate this process. During the propagation phase, a free-gas/hydrate reaction front propagates toward the seafloor, elevating salinity and temperature to three-phase equilibrium. After the reaction front breaches the seafloor, the temperature gradient in the gas chimney dissipates to background values, and salinity increases to maintain three-phase equilibrium. Ultimately, a steady state is reached in which hydrate formation occurs just below the seabed at a rate necessary to replace salt loss. We present a quantitative approach to estimate, for the steady state, the water flux and the minimum gas flux necessary for a given salinity and temperature gradient. We use this approach at the Ursa Vent in the Gulf of Mexico and show that the observed salinity and temperature gradient can be simulated with an upward flow of water (Darcy flux) of 9.5 mm yr^{-1} and a gas flow no less than 1.3 kg m^{-2} yr^{-1}. These insights improve our understanding of gas vents and highlight the importance of latent heat and salinity on gas-hydrate formation and evolution at subsurface venting sites.

Appendix A: Derivation of Steady State Hydrate Saturation and Temperature Gradient

Using conservation of mass, we express the total mass of salt in the RHSZ as ([accumulation] = [mass out] − [mass in]):

$$\frac{\partial}{\partial t}\left(\overline{\rho}\overline{C}_N\right) = -\frac{\partial}{\partial z}\left(\rho_w S_w C_{\mathrm{LN}} V_z\right), \tag{A1}$$

where $\overline{\rho}$ is average density of pore volume (sum of water plus hydrate), $\overline{C}_N$ is average composition of salt, ρ_w is density of water, S_w is water saturation, C_{LN} is composition (salt) in liquid, and V_z is liquid velocity. We assume that liquid and hydrate density are equal and that the salt mass from the average equals the salt mass in the liquid, and we define the liquid velocity as $q_w\, {S_w}^{-1}\, \phi^{-1}$, where q_w is the Darcy water flux and ϕ is porosity. This simplifies equation (A1) to

$$\frac{\partial}{\partial t}\left(S_w C_{\mathrm{LN}}\right) = -\frac{\partial}{\partial z}\left(C_{\mathrm{LN}}\frac{q_w}{\phi}\right). \tag{A2}$$

Equation (A2) establishes a relationship between water saturation and salt concentration. We assume that the system is at equilibrium salinity and that the salinity gradient is linear:

$$C_{\mathrm{LN}} = az + b, \tag{A3}$$

where a is the salinity gradient and b is the salinity of water supplied from below the RHSZ. Combining equations (A2) and (A3), assuming $S_w = 1 - S_h$ and $\partial S_w = -\partial S_h$, and considering a fixed depth, z:

$$\frac{\partial S_h}{\partial t} = \frac{q_w}{\phi}\frac{a\mathrm{d}z}{az+b}. \tag{A4}$$

Integrating

$$\int_0^z \rho_h \frac{\partial S_h}{\partial t}\mathrm{d}z = \rho_h \frac{q_w}{\phi}\ln\left(\frac{az_i + b}{b}\right), \tag{A5}$$

where z_i is depth above the base of the HSZ. Equation (A5) expresses the total mass of hydrate formed per unit time in the HSZ. At depth z_i, salinity is at the value necessary for three-phase equilibrium (C_{eq}); and at depth $z = 0$, salinity is at seawater values (C_i). Therefore, $b = C_i$ and $a = \frac{C_{\mathrm{eq}} - C_i}{z_i}$, and equation (A5) simplifies to

$$\frac{\mathrm{d}X_{h\mathrm{ADV}}}{\mathrm{d}t} = \rho_h \frac{q_w}{\phi}\ln\left(\frac{C_{\mathrm{eq}}}{C_i}\right), \tag{A6}$$

which describes the total mass of hydrate (X_h) formed for any upward (or downward) flow of water of salinity, C_i, into a zone with a critical salinity, C_{eq}.

Next, using Fick's law, the total amount of hydrate formation due to salt loss via diffusion within the boundary layer at the seafloor can be expressed as

$$\frac{\mathrm{d}X_{h\mathrm{DIFF}}}{\mathrm{d}t} = \frac{\rho_h \phi D^s_{l0} a}{\theta^2 C_{\mathrm{eq}}}. \tag{A7}$$

Combining equations (A6) and (A7), we express the total amount of hydrate added with the RHSZ due to advection of relatively fresh water from below and diffusion at the seafloor as (equation (11) from the text)

$$\frac{dX_h}{dt} = \frac{\rho_h \phi D_{l0}^s a}{\theta^2 C_{eq}} + \rho_h \frac{q_w}{\phi} \ln\left[\frac{C_{eq}}{C_i}\right]. \quad \text{(A8)}$$

The temperature gradient necessary to remove the heat flow produced from the heat added via hydrate formation can then be expressed as (equation (12) from the text)

$$\frac{dT}{dz} = \frac{Q_e + \frac{\rho_h \phi D_{l0}^s aL}{\theta^2 C_{eq}} + \rho_h \frac{q_w}{\phi} \ln\left[\frac{C_{eq}}{C_i}\right] L}{\lambda}, \quad \text{(A9)}$$

where Q_e is the background geothermal heat flow, L is the latent heat of hydrate formation, and λ is the bulk thermal conductivity. This approach neglects the heat that is transported from advection via the upward flow of water into the RHSZ. For example, for a water flux of 10 mm yr^{-1} from a source temperature of 16°C (at 440 mbsf) to the seafloor (5°C), the heat flow from advection is ~13 mW m^{-2}, which is a significant fraction of the background heat flow from conduction at Ursa (25 mW m^{-2}). However, due to poor constraints on the source temperature of the water flux, we assume that these effects are secondary and beyond the scope of the study.

Acknowledgments

We thank Royal Dutch Shell for providing three-dimensional seismic data. The University of Texas GeoFluids Consortium (supported by 12 energy companies), a JSG Corporate Partners Fellowship, and a Fulbright Fellowship (through the U.S.-Norway Fulbright Foundation) to A. Smith supported this research. We thank Marc Hesse for discussions regarding the grid spacing of the model. We thank Joe Cartwright, an anonymous reviewer, and the associate editor for constructive criticism that significantly improved the manuscript. This paper is the University of Texas Institute for Geophysics contribution #2715. Publication authorized by the Director, Bureau of Economic Geology, University of Texas.

References

Bangs, N. L. B., D. S. Sawyer, and X. Golovchenko (1993), Free gas at the base of the gas hydrate zone in the vicinity of the Chile triple junction, *Geology*, *21*(10), 905–908.

Bear, J. (1972), *Dynamics of Fluids in Porous Media*, 784 pp., American Elsevier Publishing Company, Mineola, N. Y.

Berndt, C., et al. (2014), Temporal constraints on hydrate-controlled methane seepage off Svalbard, *Science*, *343*(6168), 284–287.

Cathles, L. M., and D. F. Chen (2004), A compositional kinetic model of hydrate crystallization and dissolution, *J. Geophys. Res.*, *109*, B08102, doi:10.1029/2003JB002910.

Class, H., R. Helmig, and P. Bastian (2002), Numerical simulation of non-isothermal multiphase multicomponent processes in porous media: 1. An efficient solution technique, *Adv. Water Resour.*, *25*(5), 533–550.

Davie, M. K., and B. A. Buffett (2001), A numerical model for the formation of gas hydrate below the seafloor, *J. Geophys. Res.*, *106*(B1), 497–514, doi:10.1029/2000JB900363.

Dickens, G. R. (2003), Rethinking the global carbon cycle with a large, dynamic and microbially mediated gas hydrate capacitor, *Earth Planet. Sci. Lett.*, *213*(3–4), 169–183.

Duan, Z., N. Møller, J. Greenberg, and J. H. Weare (1992), The prediction of methane solubility in natural waters to high ionic strength from 0 to 250 °C and from 0 to 1600 bar, *Geochim. Cosmochim. Acta*, *56*(4), 1451–1460.

Egeberg, P. K. (2000), Hydrates associated with fluid flow above salt diapirs, *Proc. Ocean Drill. Program Sci. Results*, *164*, 219–228.

Evans, R., S. Stewart, and R. Davies (2007), Phase-reversed seabed reflections in seismic data: Examples related to mud volcanoes from the South Caspian Sea, *Geo Mar. Lett.*, *27*(2–4), 203–212.

Fer, I., and P. M. Haugan (2003), Dissolution from a liquid CO2 Lake disposed in the Deep Ocean, *Limnol. Oceanogr.*, *48*(2), 872–883.

Fetter, C. W. (1994), *Applied Hydrogeology*, Prentice-Hall, Upper Saddle River, N. J.

Flemings, P. B., J. G. Behrmann, C. M. John, and E. Scientists (2006), Gulf of Mexico Hydrogeology. Proc. IODP, Sci. Results, Exp. 308, 308.

Flemings, P. B., H. Long, B. Dugan, J. Germaine, C. M. John, J. H. Behrmann, D. Sawyer, and I. E. Scientists (2008), Pore pressure penetrometers document high overpressure near the seafloor where multiple submarine landslides have occurred on the continental slope, offshore Louisiana, Gulf of Mexico, *Earth Planet. Sci. Lett.*, *269*, 309–325.

Hanor, J. S., and J. A. Mercer (2010), Spatial variations in the salinity of pore waters in northern deep water Gulf of Mexico sediments: Implications for pathways and mechanisms of solute transport, *Geofluids*, *10*(1–2), 83–93.

Henry, P., M. Thomas, and M. B. Clennell (1999), Formation of natural gas hydrates in marine sediments 2. Thermodynamic calculations of stability conditions in porous sediments, *J. Geophys. Res.*, *104*(B10), 23,005–23,022, doi:10.1029/1999JB900167.

Hornbach, M. J., C. Ruppel, D. M. Saffer, C. L. Van Dover, and W. S. Holbrook (2005), Coupled geophysical constraints on heat flow and fluid flux at a salt diapir, *Geophys. Res. Lett.*, *32*, L24617, doi:10.1029/2005GL024862.

Hu, L., S. A. Yvon-Lewis, J. D. Kessler, and I. R. MacDonald (2012), Methane fluxes to the atmosphere from deepwater hydrocarbon seeps in the northern Gulf of Mexico, *J. Geophys. Res.*, *117*, C01009, doi:10.1029/2011JC007208.

Ingebritsen, S. E., W. E. Sanford, and C. E. Neuzil (2006), *Groundwater in Geologic Processes*, 2nd ed., 564 pp., Cambridge Univ. Press, Cambridge, U. K.

Kennett, J. P., K. G. Cannariato, I. L. Hendy, and R. J. Behl (2000), Carbon isotopic evidence for methane hydrate instability during quaternary interstadials, *Science*, *288*(5463), 128–133.

Kleinberg, R. L., C. Flaum, D. D. Griffin, P. G. Brewer, G. E. Malby, E. T. Peltzer, and J. P. Yesinowski (2003), Deep sea NMR: Methane hydrate growth habit in porous media and its relationship to hydraulic permeability, deposit accumulation, and submarine slope stability, *J. Geophys. Res.*, *108*(B10), 2508, doi:10.1029/2003JB002389.

Kohl, B., and H. Roberts (1994), Fossil Foraminifera from four active mud volcanoes in the Gulf of Mexico, *Geo Mar. Lett.*, *14*(2-3), 126–134.

Kvenvolden, K. A. (1993), Gas hydrates—Geological perspective and global change, *Rev. Geophys.*, *31*(2), 173–187, doi:10.1029/93RG00268.

Linga, P., N. Daraboina, J. A. Ripmeester, and P. Englezos (2012), Enhanced rate of gas hydrate formation in a fixed bed column filled with sand compared to a stirred vessel, *Chem. Eng. Sci.*, *68*(1), 617–623.

Liu, X., and P. B. Flemings (2006), Passing gas through the hydrate stability zone at southern Hydrate Ridge, offshore Oregon, *Earth Planet. Sci. Lett.*, *241*(1–2), 211–226.

Liu, X., and P. B. Flemings (2007), Dynamic multiphase flow model of hydrate formation in marine sediments, *J. Geophys. Res.*, *112*, B03101, doi:10.1029/2005JB004227.

Liu, X., and P. Flemings (2009), Dynamic response of oceanic hydrates to sea level drop, *Geophys. Res. Lett.*, *36*, L17308, doi:10.1029/2009GL039821.

MacDonald, I. R., D. B. Buthman, W. W. Sager, M. B. Peccini, and N. L. Guinasso (2000), Pulsed oil discharge from a mud volcano, *Geology*, *28*(10), 907–910.
MacDonald, I. R., W. W. Sager, and M. B. Peccini (2003), Gas hydrate and chemosynthetic biota in mounded bathymetry at mid-slope hydrocarbon seeps: Northern Gulf of Mexico, *Mar. Geol.*, *198*(1–2), 133–158.
Macdonald, I. R., M. Kastner, and I. Leifer (2005), Estimates of natural hydrocarbon flux in the Gulf of Mexico basin from remote sensing data, paper presented at European Geosciences Union, Vienna, Austria.
Marcon, Y., H. Ondreas, H. Sahling, G. Bohrmann, and K. Olu (2014), Fluid flow regimes and growth of a giant pockmark, *Geology*, *42*(1), 63–66.
Marín-Moreno, H., T. A. Minshull, G. K. Westbrook, B. Sinha, and S. Sarkar (2013), The response of methane hydrate beneath the seabed offshore Svalbard to ocean warming during the next three centuries, *Geophys. Res. Lett.*, *40*, 5159–5163, doi:10.1002/grl.50985.
McDougall, T. J. (1984), Convective processes caused by a dense, hot saline source flowing into a submarine depression from above, *Deep Sea Res. Part A Oceanogr. Res. Pap.*, *31*(11), 1287–1309.
Milkov, A. V., and R. Sassen (2002), Economic geology of offshore gas hydrate accumulations and provinces, *Mar. Pet. Geol.*, *19*(1), 1–11.
Milkov, A. V., G. R. Dickens, G. E. Claypool, Y.-J. Lee, W. S. Borowski, M. E. Torres, W. Xu, H. Tomaru, A. M. Tréhu, and P. Schultheiss (2004), Co-existence of gas hydrate, free gas, and brine within the regional gas hydrate stability zone at Hydrate Ridge (Oregon margin): Evidence from prolonged degassing of a pressurized core, *Earth Planet. Sci. Lett.*, *222*(3–4), 829–843.
Pape, T., T. Feseker, S. Kasten, D. Fischer, and G. Bohrmann (2011), Distribution and abundance of gas hydrates in near-surface deposits of the Håkon Mosby Mud Volcano, SW Barents Sea, *Geochem. Geophys. Geosyst.*, *12*, Q09009, doi:10.1029/2011GC003575.
Paull, C., W. Ussler, T. Lorenson, W. Winters, and J. Dougherty (2005), Geochemical constraints on the distribution of gas hydrates in the Gulf of Mexico, *Geo Mar. Lett.*, *25*(5), 273–280.
Paull, C. K., W. R. Normark, W. Ussler Iii, D. W. Caress, and R. Keaten (2008), Association among active seafloor deformation, mound formation, and gas hydrate growth and accumulation within the seafloor of the Santa Monica Basin, offshore California, *Mar. Geol.*, *250*(3–4), 258–275.
Phrampus, B. J., and M. J. Hornbach (2012), Recent changes to the Gulf Stream causing widespread gas hydrate destabilization, *Nature*, *490*(7421), 527–530.
Rehder, G., P. W. Brewer, E. T. Peltzer, and G. Friederich (2002), Enhanced lifetime of methane bubble streams within the deep ocean, *Geophys. Res. Lett.*, *29*(15), 1731, doi:10.1029/2001GL013966.
Reilly, M. J., and P. B. Flemings (2010), Deep pore pressures and seafloor venting in the Auger Basin, Gulf of Mexico, *Basin Res.*, *22*(4), 380–397.
Reitz, A., M. Haeckel, K. Wallmann, C. Hensen, and K. Heeschen (2007), Origin of salt-enriched pore fluids in the northern Gulf of Mexico, *Earth Planet. Sci. Lett.*, *259*(3–4), 266–282.
Rempel, A. W., and B. A. Buffett (1997), Formation and accumulation of gas hydrate in porous media, *J. Geophys. Res.*, *102*(1997), 10,151–10,164, doi:10.1029/97JB00392.
Römer, M., H. Sahling, T. Pape, A. Bahr, T. Feseker, P. Wintersteller, and G. Bohrmann (2012), Geological control and magnitude of methane ebullition from a high-flux seep area in the Black Sea—The Kerch seep area, *Mar. Geol.*, *319–322*, 57–74.
Ruppel, C., D. Lizarralde, G. Dickens, and K. Brown (2005a), Northern Gulf of Mexico Gas Hydrates (IODP #554): LDEO Site Survey Data Bank Submission Based on NSF-ODP Funded Cruise.
Ruppel, C., G. R. Dickens, D. G. Castellini, W. Gilhooly, and D. Lizarralde (2005b), Heat and salt inhibition of gas hydrate formation in the northern Gulf of Mexico, *Geophys. Res. Lett.*, *32*, L04605, doi:10.1029/2004GL021909.
Sahling, H., et al. (2009), Vodyanitskii mud volcano, Sorokin trough, Black Sea: Geological characterization and quantification of gas bubble streams, *Mar. Pet. Geol.*, *26*(9), 1799–1811.
Sassen, R., S. T. Sweet, A. V. Milkov, D. A. DeFreitas, and M. C. Kennicutt II (2001), Thermogenic vent gas and gas hydrate in the Gulf of Mexico slope: Is gas hydrate decomposition significant?, *Geology*, *29*(2), 107–110.
Sawyer, D., P. B. Flemings, R. C. Shipp, and C. D. Winker (2007), Seismic geomorphology, lithology, and evolution of the late Pleistocene Mars-Ursa turbidite region, Mississippi Canyon area, northern Gulf of Mexico, *AAPG Bull.*, *91*(2), 215–234.
Schmidt, M., C. Hensen, T. Mörzb, C. Müller, I. Grevemeyer, K. Wallmann, S. Mau, and N. Kaul (2005), Methane hydrate accumulation in "Mound 11" mud volcano, Costa Rica forearc, *Mar. Geol.*, *216*(1–2), 83–100.
Seldon, B., and P. B. Flemings (2005), Reservoir pressure and seafloor venting: Predicting trap integrity in a Gulf of Mexico deepwater turbidite minibasin, *AAPG Bull.*, *89*(2), 193–209.
Shipley, T. H., M. H. Houston, R. T. Buffler, F. J. Shaub, K. J. McMillen, J. W. Ladd, and J. L. Worzel (1979), Seismic evidence for widespread possible gas hydrate horizons on continental slopes and rises, *AAPG Bull.*, *63*(12), 2204–2213.
Sloan, E. D. (1998), *Clathrate Hydrates of Natural Gases*, 2nd ed., 705 pp., Marcel Dekker, New York.
Smith, A. J., P. B. Flemings, and P. M. Fulton (2014), Hydrocarbon flux from Natural Deepwater Gulf of Mexico vents, *Earth Planet. Sci. Lett.*, *395*, 241–253.
Torres, M. E., K. Wallmann, A. M. Tréhu, G. Bohrmann, W. S. Borowski, and H. Tomaru (2004), Gas hydrate growth, methane transport, and chloride enrichment at the southern summit of Hydrate Ridge, Cascadia margin off Oregon, *Earth Planet. Sci. Lett.*, *226*(1–2), 225–241.
Tréhu, A. M., P. B. Flemings, N. L. Bangs, J. Chevallier, E. Gràcia, J. E. Johnson, C. S. Liu, X. Liu, M. Riedel, and M. E. Torres (2004), Feeding methane vents and gas hydrate deposits at south Hydrate Ridge, *Geophys. Res. Lett.*, *31*, L23310, doi:10.1029/2004GL021286.
Turner, J. S., and L. B. Gustafson (1978), The flow of hot saline solutions from vents in the sea floor; some implications for exhalative massive sulfide and other ore deposits, *Econ. Geol.*, *73*(6), 1082–1100.
Westbrook, G. K., et al. (2009), Escape of methane gas from the seabed along the West Spitsbergen continental margin, *Geophys. Res. Lett.*, *36*, L15608, doi:10.1029/2009GL039191.
Winters, W. J., T. D. Lorenson, and C. K. Paull (2007), Initial Report of the IMAGES VIII/PAGE 127 Gas Hydrate and Paleoclimate Cruise on the RV Marion Dufresne in the Gulf of Mexico, 2-18 July 2002: *U.S. Geol. Surv. Open File Rep., 2004–1358*.
Wood, W. T., J. F. Gettrust, N. R. Chapman, G. D. Spence, and R. D. Hyndman (2002), Decreased stability of methane hydrates in marine sediments owing to phase-boundary roughness, *Nature*, *420*(6916), 656–660.
Yousif, M. H., H. H. Abass, M. S. Selim, and E. D. Sloan (1991), Experimental and theoretical investigation of Methane-Gas-Hydrate dissociation in porous media, *SPE Reservoir Eng.*, *6*(1), 69–76.
Zatsepina, O. Y., and B. A. Buffett (2003), Nucleation of gas hydrate in marine environments, *Geophys. Res. Lett.*, *30*(9), 1451, doi:10.1029/2002GL016802.